Migration behaviour of Europium implanted into single crystalline 6H-SiC

Tshegofatso Magapeletse Mohlala

Submitted in partial fulfilment of the requirements

for the degree

Master of Science (MSc) in Physics

in the Faculty of Natural and Agricultural Sciences

University of Pretoria

Supervisor: Dr TT Hlatshwayo

Co supervisor: Prof JB Malherbe

July 2017

UNIVERSITY OF PRETORIA

DECLARATION OF ORIGINALITY

This form must be submitted together with the copies of the dissertation/thesis/essay for the examiners.

TITLE: Mr

REGISTRATION NUMBER: 10064487

Full names: Tshegofatso Magapeletse Mohlala

STATEMENT BY CANDIDATE

I declare that the dissertation, which I hereby submit for the degree MSc in Physics at the University of Pretoria, is my own work and has not been previously submitted by me for a degree at another university.

I am aware that, should the dissertation be accepted, I must submit the additional copies as required by the relevant regulations at least six weeks before the next graduation ceremony, and that the degree will not be conferred if this requirement is not fulfilled.

SIGNATURE:…….

DATE:…….....

Summary

The release of radioactive fission products during nuclear energy reactor operation imposes a serious danger to personnel's health and the environment. In a modern Pebble Bed Modular Reactor (PBMR) TristructuralIsotropic (TRISO) fuel, silicon carbide (SiC) is used as the main barrier to fission products (FPs). TRISO particles retain most of the FPs well with the exception of silver (Ag), strontium (Sr) and Europium (Eu) during operation. The migration behavior of Ag in SiC has been thoroughly investigated over decades with fewer investigations done on the migration behavior of Sr and Eu.

In this study the migration behavior of Europium (Eu) implanted into 6H-SiC was investigated using Rutherford backscattering spectrometry (RBS), RBS in a channeling mode (RBS-C) and scanning electron microscopy (SEM). Eu ions of 360 keV were implanted into 6H-SiC at 600°C to a fluence of 1×10^{16} cm^{-2}. This high temperature was chosen because PBMR reactors are designed to operate at high temperatures.

The implanted samples were sequentially annealed at temperatures ranging from 1000 to 1400 °C, in steps of 100 °C for 5 hours. RBS-C showed that implantation of Eu into 6H-SiC at 600 °C retained crystallinity with some radiation damage. Reduction of the radiation damage retained after implantation, already took place after annealing at 1000 °C. This annealing of radiation damage progressed with increasing annealing temperature up to 1400 °C. A shift of Eu towards the surface took place after annealing at 1000 °C. This shift became more pronounced and was accompanied by loss of Eu from the surface at annealing temperatures >1000 °C. This shift was accompanied by broadening of Eu peak, indicating Fickian diffusion occurring after annealing at temperatures > 1100 °C. The migration of Eu occurring concurrently with the annealing of radiation damage was explained by trapping and de-trapping of Eu by radiation damage. The diffusion coefficients were found to be 1.56×10^{-18} m^2s^{-1} and $2.98\times 10^{-18}m^2s^{-1}$at 1200 °C and 1300 °C respectively.

Acknowledgements

I would like to thank my project supervisor Dr TT Hlatshwayo and my co-supervisor Prof JB Malherbe for their support and guidance throughout the project. I was always welcome to enter their offices whenever I had a question or any discussion about my work. I would also like to thank all my fellow students, members of nuclear materials group and friends for their motivation and support.

I would also like to thank my family, my parents (Kelly and Malesela Mohlala) and my three brothers for their trust in me, support and encouragement

The financial support from the National Research Foundation (NRF) of South Africa is hereby appreciated.

I thank God for nourishing my memory with his great news, promises and motivations, I thank him for keeping me away from life threatening situations and protecting me at all times.

Table of Contents

List of Figures

Chapter 1

INTRODUCTION

The world today is facing great energy-related challenges. The need to find a clean and sustainable source of energy to replace fossil fuel has reached a point of no return. Despite the challenge faced due to the availability of petroleum in the future, the emission of greenhouse gases by coal, oil and gas burning imposes a high health risk to the environment thereby polluting the atmosphere. The total World Energy Consumption by Source (2011) indicates in the whole world that 78.2% of fossil fuel is used, 19% is renewable energy and with the remaining 2.8% being nuclear energy [1].

The environmental impact of nuclear power results from the nuclear fuel cycle, operation and the effects of nuclear accidents. While coal is still used as a major source of energy generation in most countries like ours (South Africa), the greenhouse gas emission from nuclear fission reactors is much smaller compared the greenhouse gas emission associated with coal, oil and gas. Therefore, the health risks from nuclear energy are minimized as compared to those associated with coal. There is however a catastrophic risk potential associated with nuclear reactors if nuclear fuel containment fails. This can be brought about by over-heated fuels melting and releasing large quantities of fission products to the environment. Long-lived radioactive wastes, including spent nuclear fuel, must be contained and isolated from the environment. Most nuclear plants store used fuel in steel-lined, concrete pools filled with water or in massive airtight steel or concrete and steel canisters. Figure 1.1 shows a spent fuel pool. The water in the pools acts as a natural barrier for radiation. The spent fuel assemblies are also moved to pools of water to absorb the heat energy released by radioactive decay processes. They are kept in racks in the pool and water is continuously circulated to draw heat away from the rods. During an accident at Fukushima Daiichi in Japan, the used fuel in pool storage survived an earthquake and tsunami without significant damage which indicated the robust design of storage pools [2].

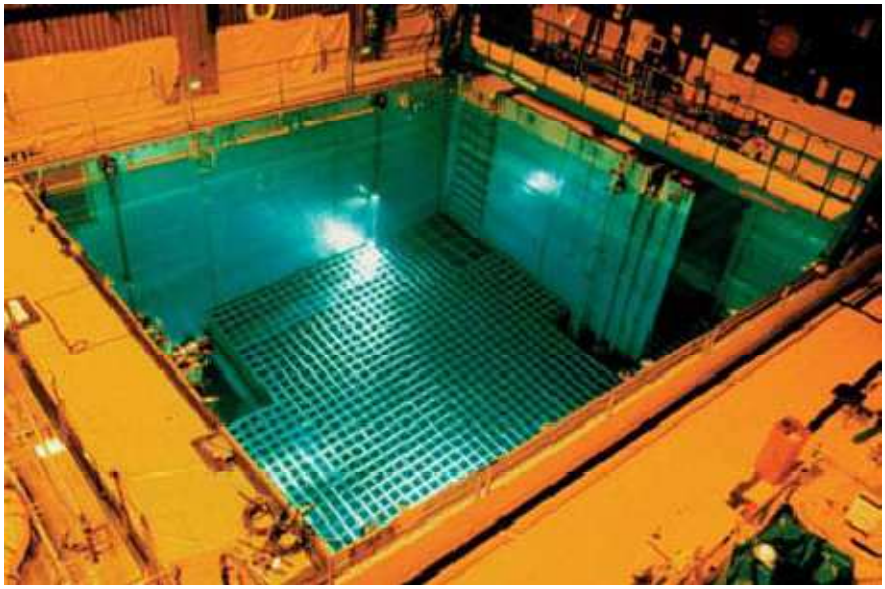

Figure 1.1: *An image of a spent fuel pool filled with water. Taken from reference [3].*

The dry casks store the fuel which had spent a period of five years in the fuel pools. At that stage, the fuel is cool enough to be stored in the dry casks, especially because the dry casks are placed outdoors on concrete pads. An image of dry casks used is shown in Figure 1.2.

Figure 1.2: *An image showing dry casks placed on concrete pads. Taken from reference [3].*

The 1974 Three Mile Island accident, the 1986 Chernobyl disaster and the issue of nuclear radiation material disposal caused considerable public opposition and ended the rapid growth of global nuclear power capacity. Quite recently, the release of radioactive materials following the 2011 Japanese tsunami which damaged the Fukushima Nuclear Power plant resulted in people being evacuated from a 20 km exclusion zone set up around the power

plant. This has resulted in the rebirth of public outcry in the safety of nuclear energy [4]. On the other hand all these events have accelerated the necessity of thorough investigations on the materials used in the nuclear reactors to improve safety.

Modern Generation IV nuclear reactors operate at high temperatures of about 900 °C and above. During nuclear reactor accidents, the temperature of the core can rise significantly above 1000 °C. Thus, the design of the containment of fission products must be able to resist both the operation temperatures and the accident temperatures. One way to achieve this, is to invest in intensive research on the properties and behavior of the materials used in the construction of the reactor cores and on fuel particle containment, and make some changes and improvements where necessary. In earlier reactors, such as those of the Chernobyl, the reactor had not been encased by any kind of hard containment vessel/material [5]. During the Chernobyl disaster, the reactor suffered a catastrophic power increase, leading to explosions in its core. This dispersed large amounts of radioactive fuel and core materials into the atmosphere and ignited the combustible graphite moderator [5].

The containment of nuclear fuel is very important in the design of the reactor itself. In the Generation IV nuclear reactors such as Pebble Bed Modular Reactor (PBMR), the fuel kernels (UO_2) are covered by four different layers. The schematic diagram of a fuel particle is shown in Figure 1.3

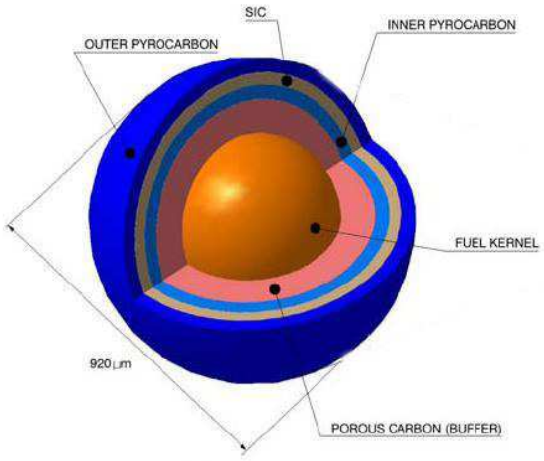

Figure 1.3: *A schematic diagram of a TRISO fuel particle. Taken from reference [6].*

These four successive layers are, a graphite buffer, an inner layer of pyrocarbon, a layer of silicon carbide (SiC) and an outer layer of pyrocarbon. The main function of the low density PyC layer (also known as the buffer layer) is to attenuate the fission recoils and to provide voids for gaseous fission products and carbon monoxides that are produced. The inner PyC retains gaseous fission products, the SiC layer retains solid fission products or acts as a barrier to solids fission products and provides adequate structural stability during compact fabrication. The high-density outer PyC protects silicon carbide layer mechanically and chemically. These coated fuel particles are called TRISO (Tristructural Isotropic) particles. About 15000 of these 0.92 mm particles are packed together in a 60 mm fuel sphere (pebble) as shown in Figure 1.4,

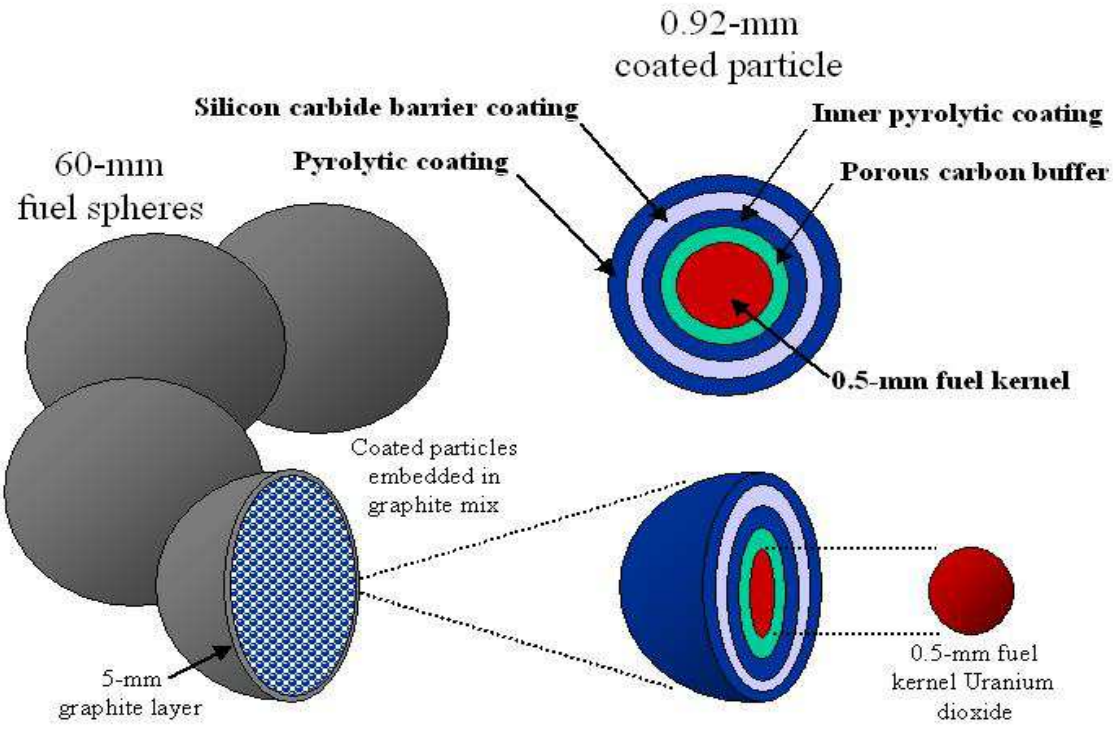

Figure 1.4: *An illustration of the fuel in a PBMR technology (Generation IV modern reactors). Taken from reference [7].*

Nuclear reactors use uranium as a fuel to generate heat/energy via a physical process called fission. This process involves the splitting of atoms of uranium. There are two main naturally occurring isotopes of uranium, namely, U-238 and U-235. When a neutron is absorbed by a fissile U-235 as shown in Figure 1.5, U-236 is formed which is unstable. U-236 splits into two different fission products and neutrons. During this process a lot of heat energy is released.

If the released neutrons are allowed to further react with other U-235 atoms, more energy would be released by a process called chain reaction.

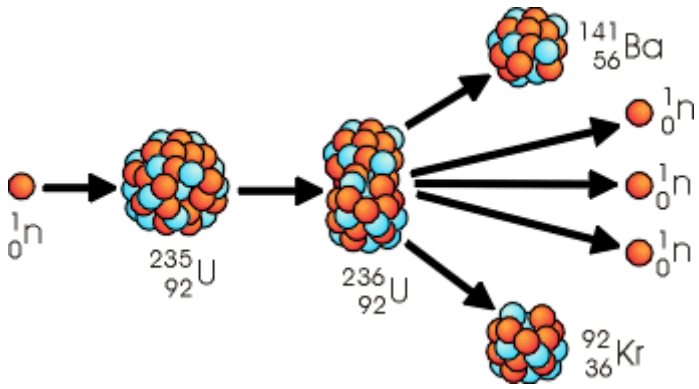

Figure 1.5: *Illustration of a uranium fission reaction. Taken from reference [8].*

Some of the produced fission products (FPs) are radioactive and are harmful to humans and nature.

TRISO particles retain most of the FPs well with the exception of silver (Ag), strontium (Sr) and europium (Eu) during reactor operation [9, 10]. The Generation IV Reactor Program includes high temperature reactors (HTR's) operating at temperatures significantly above 1000 ºC to enhance their efficiency, especially in view of process heat applications for hydrogen generation [11]. Less information is available on the migration behaviour of fission products at the temperatures above 1000 ºC. Our group at University of Pretoria has recently investigated the migration of some fission products above 1000 ºC [12-19]. Extensive investigations have been performed in the migration behaviour of Ag in SiC in the temperatures below and above 1000 ^{o}C [5].

Very little has been reported on the migration behaviour of Eu in SiC [1, 6]. It has only been recently investigated in the entire TRISO particle, leaving doubts in performance of each layer [20]. Europium is a highly reactive metal which react with Si to form a stable silicide and with carbon to form a stable carbide. Consequently, one would expect that at high temperatures (like those used in this study) and at the concentration levels used in this study (i.e. a maximum 2 atomic percent) that Eu would dissolve in the SiC. Europium is toxic to lungs and mucous membranes if inhaled, it is corrosive and an irritant to skin [21]. In the reported studies of the migration behaviour of Eu in SiC, the influence of radiation damage

has not been investigated. In the nuclear reactor environment, SiC is continuously exposed to irradiation, hence the influence of radiation damage on the migration of Eu in SiC is crucial.

In this study, we report on the investigation of influence of radiation damage in the migration behaviour of Eu implanted into 6H-SiC to a fluence of 1×10^{16} cm^{-2}. The radiation damage retained after implantation played a major role in the migration behaviour of implanted Eu.

Silicon carbide is a compound of equal amounts of tetrahedral bonded silicon and carbon with the chemical formula SiC, A silicon atom is bonded to four carbon atoms or a carbon atom bonded to four Si atoms. This compound exists in more than 200 structural forms. In this project the single crystalline silicon carbide ((α)6H-SiC) is used. The alpha silicon carbide (α-SiC) is the most commonly encountered polytype of SiC. It is formed at temperatures greater than 1700 °C and has a hexagonal crystal structure [22]. In Figure 1.6 is the structure of (α)6H-SiC:

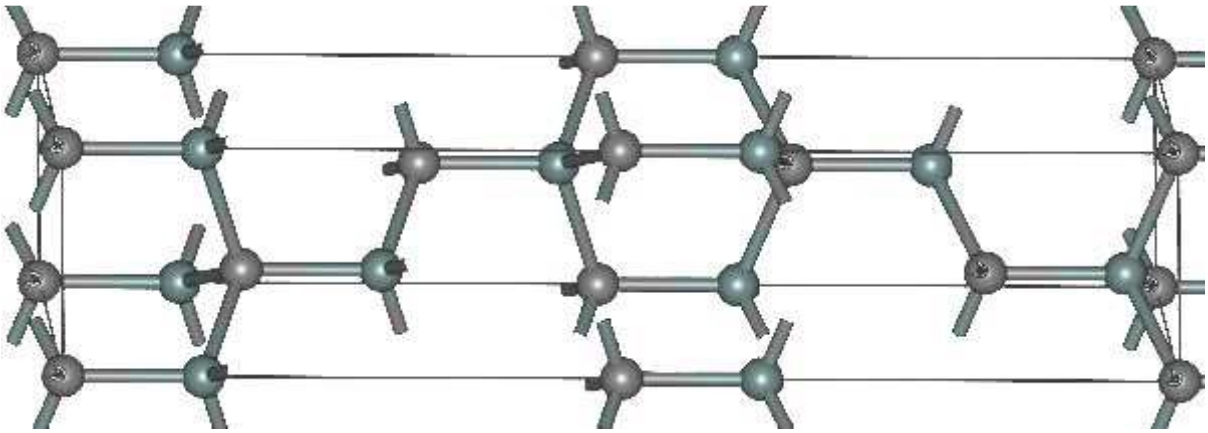

Figure 1.6: *The structure of (α)6H-SiC. Taken from reference [21].*

6H-SiC has a stacking sequence of ABCABC, two thirds and one third hexagonal bods. A layer is said to be in hexagonal (h) configuration if it is surrounded on either side by layers of the same type. It is in cubic (c) configuration if it is surrounded by layers of different type on either side [23], see Figure 2.3 for a clear distinction. The ABCABC stacking sequence of 6H-SiC can therefore be described as hcchcc. This stacking sequence makes 6H-SiC a hard material.

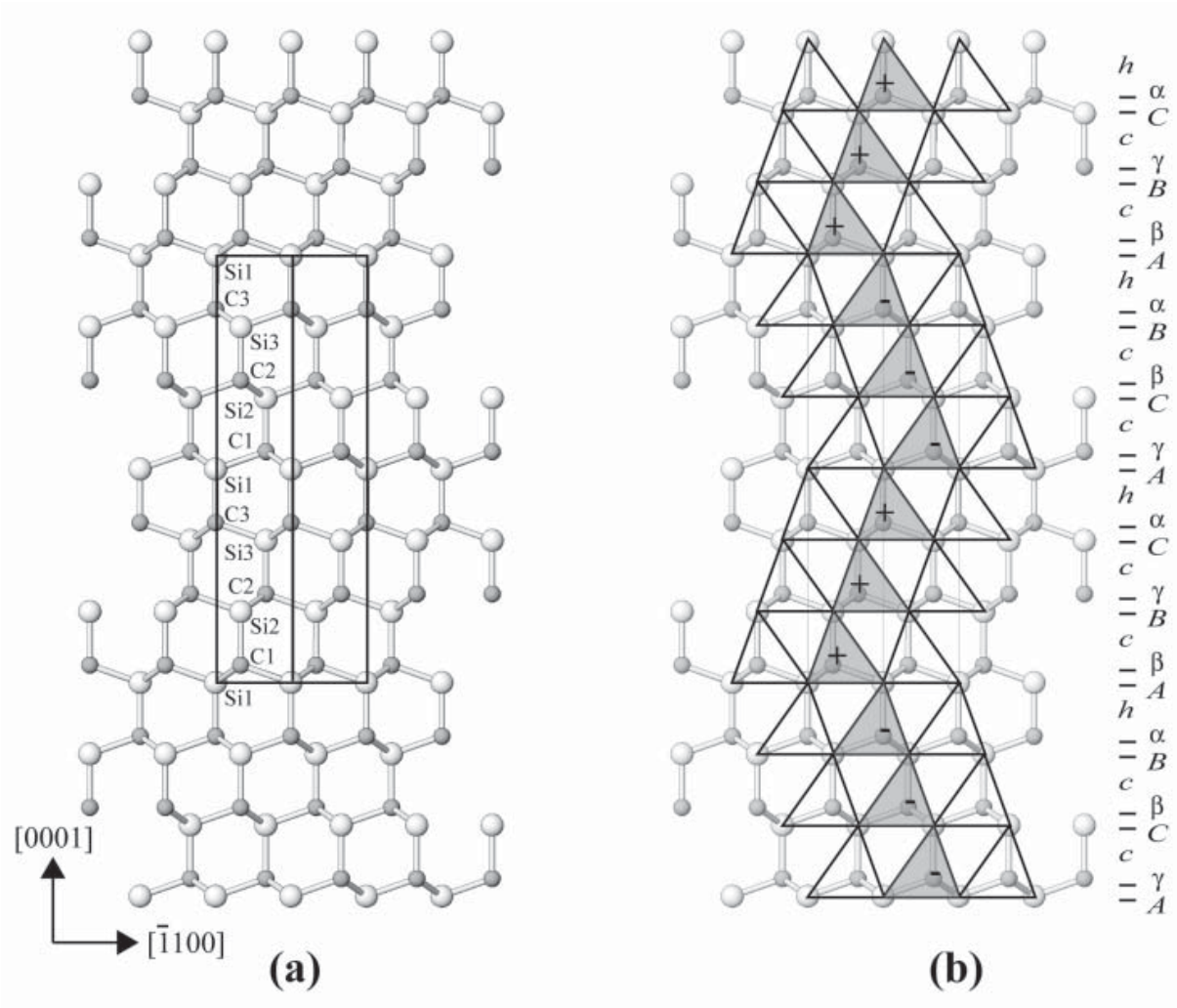

Figure 1.7: ***(a)*** *The refined 6H-SiC structure as projected on the (1120) plane.* ***(b)*** *Same as before, but with superposition of the stacking scheme. Taken from raference [23].*

Among the other properties of SiC are; a large band-gap for high-temperature operation and radiation resistance, high saturated electron velocity for high-frequency operation, high mechanical hardness, significantly higher thermal conductivity for thermal management of high power devices, etc. The first three properties make SiC a material of choice as the main barrier layer in a TRISO particle. The high sublimation temperature of SiC (of about 2700 ˚C) makes it more useful for the applications in a very high temperature environment. SiC is used in electronic materials as a semiconductor material because of its high thermal conductivity. Silicon carbide does not melt at any known pressure and it is also highly chemically inert [22].

The rest of this dissertation is organised as follows:

Chapter 2 discusses the theory of diffusion, the diffusion mechanisms and the mathematics thereof. In chapter 3, ion implantation is discussed from ion interaction to ion channelling. Chapter 4 describes the methodology used in the project, Rutherford Backscattering Spectrometry (RBS), channelling mode of it (RBS-C) and scanning electron spectrometry (SEM). Chapter 5 describes the experimental procedure, in chapter 6 the results of all the experiments are discussed and then chapter 7 gives the conclusion.

References

[1] world-nuclear. (n.d.). *World Nuclear Association*. [online] Available at: http://www.world-nuclear.org/information-library/nuclear-fuel-cycle/nuclear-power-%20reactors/generation-iv-nuclear-reactors.aspx [Accessed 17 Jul. 2016].

[2] Nei.org. (n.d.). *At-Reactor Storage of Used Nuclear Fuel - Nuclear Energy Institute*. [online] Available at: https://www.nei.org/Issues-Policy/Used- Nuclear-Fuel-Management/At-Reactor-Storage-of-Used-Nuclear-Fuel [Accessed 20 Jul. 2016].

[3] Spent Nuclear Fuel Pools in the U.S. (2011). *Institute for Policy Studies*. [online] Available at: http://www.ips-dc.org [Accessed 4 Jul. 2016].

[4] Library, W. (2016). | *World Public Library - eBooks | Read eBooks online.* [online] Worldlibrary.org. Available at: http://www.worldlibrary.org/articles/environmental_impact_of_nuclear_power#Enviro nme ntal_effects_of_accidents_and_attacks [Accessed 31 May 2016].

[5] wikipedia.org. (2016). *Chernobyl Disaster*. [online] Available at: http://en.wikipedia.org/wiki/Chenobyl-disaster [Accessed 9 Jul. 2016].

[6] Davis, M., Balog, F., Nemanich, G., Katsaros, A., Ogden, J., Niedzwiecki, A. and Serfass, J. (2002). National Hydrogen Energy Roadmap. *National Energy Policy*.

[7] Nuclearpoweryesplease.org. (2016). *January | 2012 | Nuclear Power? Yes Please*. [online] Available at: http://nuclearpoweryesplease.org/blog/2012/01/ [Accessed 28 Jan. 2016].

[8] Classroom Physics Demos. *MouseTrap Reactor*. [online] Available at: https://demos.smu.ca/index.php/demos/modern/30-mousetrap-reactor [Accessed 27 Oct. 2015].

[9] Malherbe, J.B., Friedland, E. and van der Berg, N.G. (2008). Ion beam analysis of materials in the PBMR reactor.*Nuclear Instruments and Methods in Physics Research Section B: Beam Interactions with Materials and Atoms*, 266(8), pp.1373-1377.

[10] Davis, M., Balog, F., Nemanich, G., Katsaros, A., Ogden, J., Niedzwiecki, A. and Serfass, J. (2002). National Hydrogen Energy Roadmap. *National Energy Policy*.

[11] Internation Atomic Energy Agency, (1997). Fuel performance and fission product behaviour in gas cooled reactors. [online] Available at: http://www-pub.iaea.org/books/IAEABooks/5633/Fuel-Performance-and-FissionProductBehaviour-in-Gas-Cooled-Reactors [Accessed 8 Feb. 2017].

[12] Friedland, E., Malherbe, J.B., van der Berg, N.G., Hlatshwayo, T.T., Botha, A.J, Wendler, E. andWesch, W. (2009). Study of silver diffusion in silicon carbide. *Journal of Nuclear Materials*, 389(2), pp.326-331.

[13] Friedland, E., van der Berg, N.G., Malherbe, J.B., Kuhudzai, R.J., Botha, A.J., Wendler, E. and Wesch, W. (2010). Study of iodine diffusion in silicon carbide. *Nuclear Instruments and Methods in Physics Research Section B: Beam Interactions with Materials and Atoms*, 268(19), pp.2892-2896.

[14] Friedland, E., van der Berg, N.G., Malherbe, J.B., Hanke, J., Barry, J., Wendler, E. and Wesch, W. (2011). Investigation of silver and iodine transport through silicon carbide layers prepared for nuclear fuel element cladding. *Journal of Nuclear Material*, 410, pp.24-31.

[15] Friedland, E., van der Berg, N.G., Malherbe, J.B., Wendler, E. and Wesch, W. (2012). Influence of radiation damage on strontium and iodine diffusion in silicon carbide. *Journal of Nuclear Materials*, 425(1-3), pp.205-210.

[16] Friedland, E., Hlatshwayo, T.T, van der Berg, N.G. and Mabena, M.C. (2015). Influence of radiation damage on krypton diffusion in silicon carbide. *Nuclear Instruments and Methods in Physics Research Section B: Beam Interactions with Materials and Atoms*, 354, pp.42-46.

[17] Friedland, E., van der Berg, N.G., Hlatshwayo, T.T., Kuhudzai, R.J., Malherbe, J.B.,Wendler, E. and Wesch, W. (2012). Diffusion behavior of cesium in siliconcarbide at$T>1000°C$.*Nuclear Instruments and Methods in Physics Research Section B: Beam Interactions with Materials and Atoms*, 286, pp.102-107.

[18] Friedland, E., Hlatshwayo, T.T. and van der Berg, N.G. (2013). Influence of radiation damage on diffusion of fission products in silicon carbide. *physics status solidi(c)*, 10(2), pp.208-215.

[19] Njoroge, E., Theron, C.C., Malherbe, J.B. and Ndwandwe, O. (2014). Kinetics of solid-state reactions between zirconium thin film and silicon carbide at elevated temperatures. *Nuclear Instruments and Methods in Physics Research Section B: Beam Interactions with Materials and Atoms*, 332, pp.138-142.

[20] Demkowicz, P., Reber, E., Scates, D., Scott, L. and Collin, B. (2015). First high temperature safety tests of AGR-1 TRISO fuel with the Fuel Accident Condition Simulator (FACS) furnace. *Journal of Nuclear Materials*, 464, pp.320-330.

[21] Sciencelab.com. *Material safety data sheet, Chemicals and laboratory equipment*. [online] Availableat: http://www.sciencelab.com/msds.php?msdsId=9924008 [Accessed 25 Jan. 2016].

[22] En.wikipedia.org. *Silicon carbide*. [online] Available at: http://en.wikipedia.org/wiki/silicon_carbide [Accessed 10 May 2016].

[23] Capitani, G.C., Di Pierro, S. and Tempesta, G. (2007). The 6H-SiC structure model: Further refinement from SCXRD data from a terrestrial moissanite. *American Mineralogist*, 92(2-3), pp.403-407.

Chapter 2

DIFFUSION

This study focuses on the migration behaviour of Eu ions implanted into single crystalline 6H-SiC. The migration of implanted Eu in SiC might be due to diffusion. In this chapter the difference between single crystalline (used in this study) and polycrystalline material is firstly highlighted followed by the diffusion process in single crystalline materials.

2.1. Single crystalline material (6H-SiC) and polycrystalline material.

A single crystalline material is a material in which the crystal lattice of the entire sample is continuous and unbroken to the edges of the sample, with no grain boundaries. It differs from the polycrystalline in that the polycrystalline material has many grains of varying size and orientation as illustrated in Figure 2.1.

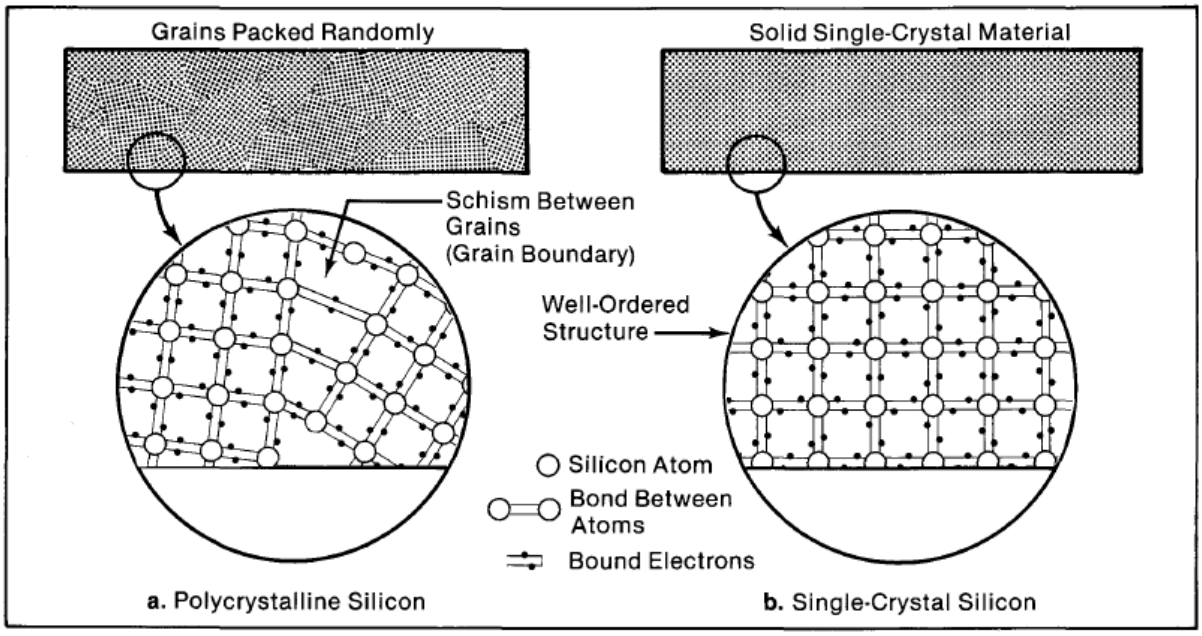

Figure 2.1: *An illustration of the difference between a polycrystalline and a single crystalline materials. Taken from reference [1].*

2.2. Diffusion

Diffusion is a phenomenon of material transport by atomic motion from a region of high concentration to a region of low concentration. This phenomenon is demonstrated in Figure 2.2. where atoms of type A and type B are on the right and left respectively.

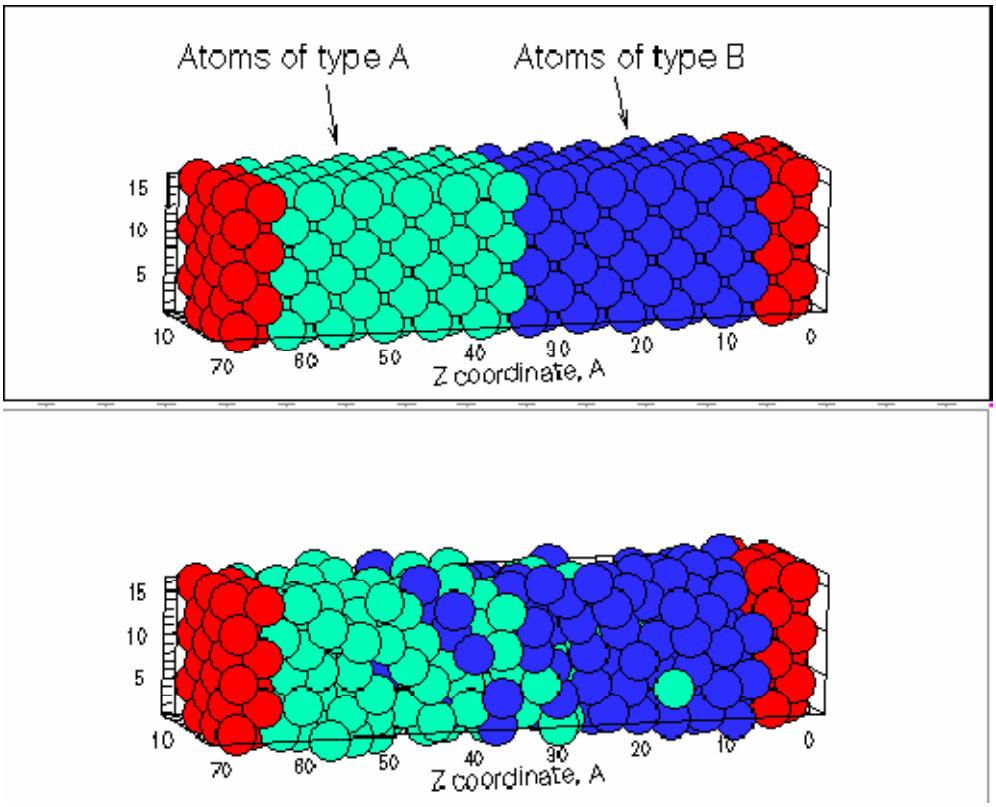

Figure 2.2: *The results of an atomic diffusion. Taken from reference [2].*

For diffusion to occur, the atoms should have enough energy to overcome energy barriers to atomic motion. Normally, this energy is obtained from thermal energy i.e. increasing the temperature/annealing. Many reactions and processes that are important in the analysis of materials depend on mass transfer within a specific solid [3]. This is achieved by diffusion. In solid materials atoms are in constant vibrations about their lattice positions. For an atom to change position, it must have sufficient energy to break bonds joining it with its neighbouring atoms. In a material of interest, diffusion can occur via different mechanisms. In this study, only the diffusion mechanisms that occur in single crystalline will be mainly discussed.

In a single crystalline material, diffusion may occur mainly via: vacancy diffusion mechanism which involves the interchange of an atom from a normal lattice position to an adjacent vacant lattice site as demonstrated in Figure.2.3 and interstitial diffusion mechanism

which involves atoms migrating from an interstitial position to a neighbouring one that is empty, Figure.2.4.

2.2.1. Diffusion Mechanisms in single crystalline material

To jump from lattice site to lattice site and to cause the necessary lattice distortions during jump, atoms need energy to break bonds with their neighboring atoms as mentioned already. This energy comes from the thermal energy of atomic vibrations (Eav~KBT). The direction of flow of atoms is opposite the direction flow of the vacancy see Figure 2.3. Therefore, the rate of this kind of diffusion depends mainly on the number of vacancies available.

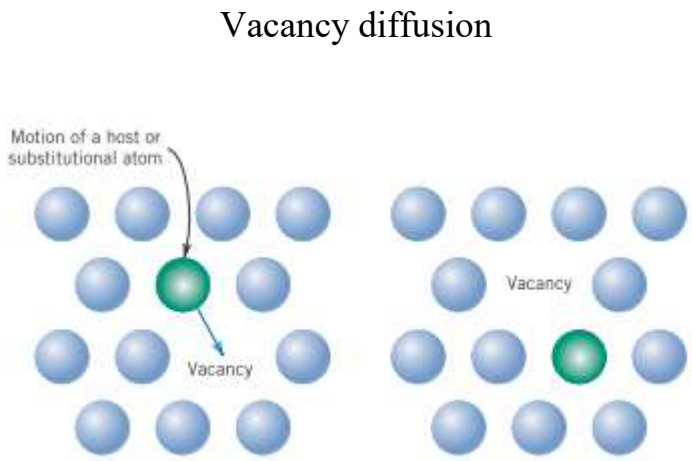

Figure 2.3: *Movement of an atom from a lattice point to a vacant site. Taken from reference [3].*

Interstitial diffusion

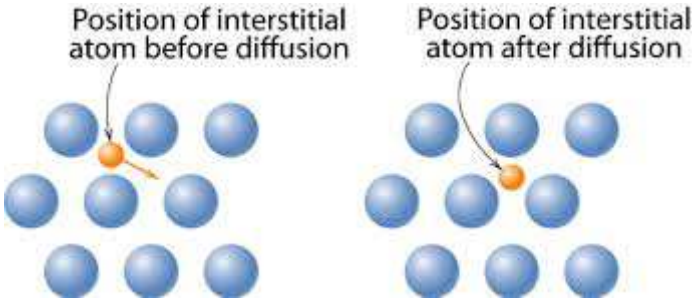

Figure 2.4: *Schematic representations of vacancy diffusion and interstitial diffusion. Taken from reference [3].*

In interstitial diffusion (shown in Figure 2.4) an atom migrates from an interstitial position to neighbouring empty site (another interstitial site) . Interstitial diffusion is generally faster than vacancy diffusion due to the fact that bonding of interstitials to the surrounding atoms is normally weaker and there are more interstitial sites than there are vacancy sites to jump to. Smaller atoms can diffuse between interstices in host atoms [2]. For larger atoms such as Eu, the interstices will be occupied at the expense of lattice distortion i.e. the host atoms surrounding Eu will be pushed outwards.

2.3. Laws of diffusion

2.3.1. Diffusion Flux

The flux (J) of diffusing atoms is used to determine the rate of diffusion. It is defined as the number of atoms diffusing through a unit area per unit time (atoms/m^2.s). $\frac{dn}{dt}$ is the number of atoms crossing area A per unit time, A is the cross-sectional area shown as a square in Figure. 2.5. The arrow in the Figure indicates the flow direction.

$$J = \frac{1}{A}\frac{dn}{dt} \qquad (2.1)$$

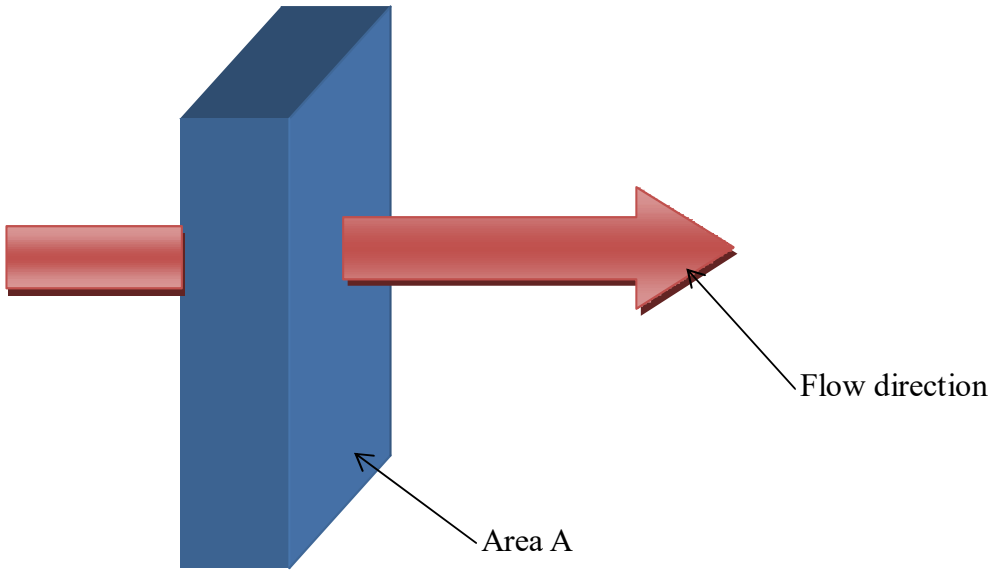

Figure 2.5: *Illustration of diffusion flux.*

2.3.2. Fick's first law

The diffusion flux along direction x is proportional to the concentration gradient:

$$J \propto \frac{dc}{dx} \rightarrow J = -D\frac{dC}{dx} \tag{2.2}$$

where D is a constant of proportionality known as the diffusion coefficient, and dC/dx is the concentration gradient. The minus sign in the equation implies that the diffusion is opposite to the concentration gradient.

2.3.3. Non-Steady state (Fick's second law)

In reality, the concentration profile and the concentration gradient are changing with time. In such cases the changes of the concentration profile can be described by a differential equation:

$$\frac{\partial C}{\partial t} = \frac{\partial}{\partial x}\left(D\frac{\partial C}{\partial x}\right) = D\frac{\partial^2 C}{\partial x^2} \tag{2.3}$$

The solution to this equation is a concentration profile as a function of time, C(x,t).

Using the following boundary conditions;

- C (x = 0) = C_s, constant, fixed

- C (x = 0) = C_0, corresponding to the original concentration of the dopant existing in the phase at x = ∞.

We get the following solution [4]:

$$C(x,t) = C_s - (C_s - C_0)erf\left(\frac{2}{2\sqrt{Dt}}\right) \tag{2.4}$$

Where C_s is the fixed amount of dopant per area, C_0 is the original concentration, D is the diffusion coefficient.

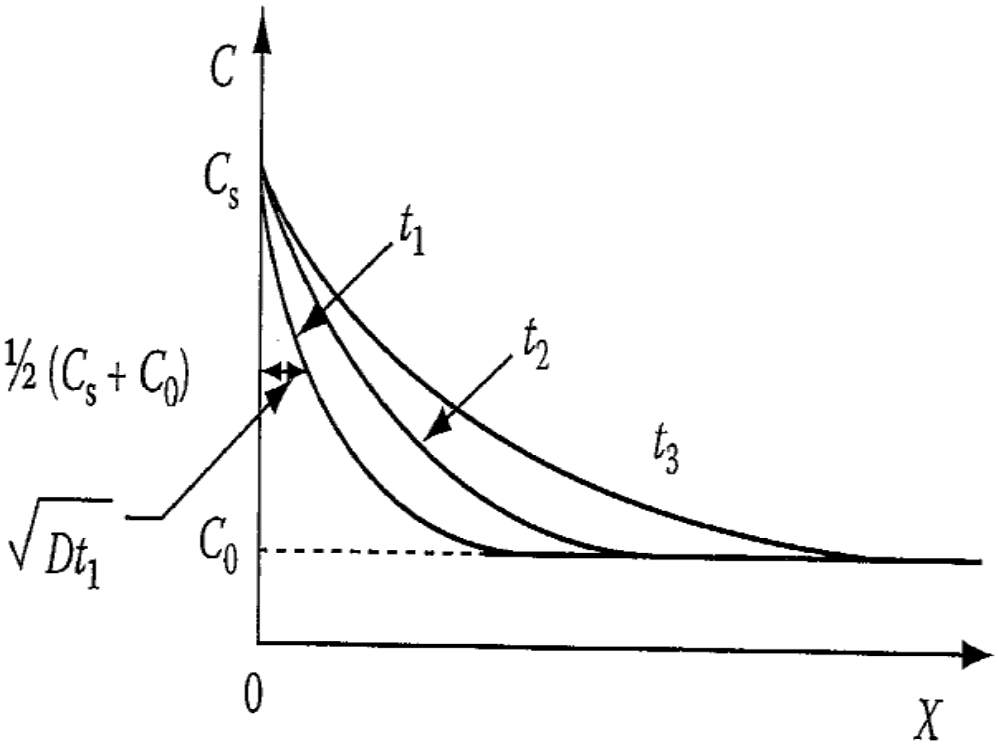

Figure 2.6: *Illustration of Fick's second law, C (ions/cm^2.s) and x (cm). Taken from reference [4].*

The dopant thickness is defined as the diffusion depth at 1/2(C_s + C_0) = √Dt.

At time t_1, in a shorter period of time, the species already diffuses in to the material, at time t_2 it continues to diffuse more deeper into the material and given a long period of time at t_3 the species is able to diffuse even more deeper into the material as can be seen by the broadening concentration profile from t_1 to t_3.

2.3.4. Diffusion Coefficient

Fick's diffusion equation for the dilute limit leads to a particularly simple solution provided the original profile at time t_0=0 is a Gaussian distribution [5], and the concentration profile after annealing for time t stays as normal distribution

$$C(x,t) = K[\pi Dt]^{-1/2} \exp\left(-\frac{x^2}{4Dt}\right) \tag{2.5}$$

where K is an adjustable constant. Defining the width of the profile after some time t, W(t), as the full width at half maximum *(FWHM*), the relationship between the profile width W(t) and the profile width at time t=0 ,W(0), is given by

$$[W(t)]^2 = 4Dt\ln(2) + [W(0)]^2 \tag{2.6}$$

The diffusion coefficient D is directly obtained from the slope of a curve of $[W(0)]^2$ versus annealing time at constant temperature.

In a limited temperature range the diffusion coefficient depends exponentially on temperature. This dependence has important consequences with regard to material behaviour and is given by Arrhenius equation:

$$D = D_0 \exp\left(-\frac{E_a}{k_B T}\right) \tag{2.7}$$

D_0 is a temperature-independent pre-exponential (m^2/s), E_a is the activation energy for diffusion (*J/mol*), K_B is the Boltzmann's constant and T is the absolute temperature (*K*). Equation 2.7 can be rewritten as:

$$\ln D = \ln D_0 - \frac{E_a}{K_B}\left(\frac{1}{T}\right) \tag{2.8}$$

From this equation, it is quite clear that the activation energy E_a and the pre-exponential D_0 can be estimated from a graph of ln$D$ versus 1/T. A typical example of such graph is shown in Figure 2.8. From the slope and x intercept, E_a and D_0 can be deduced respectively.

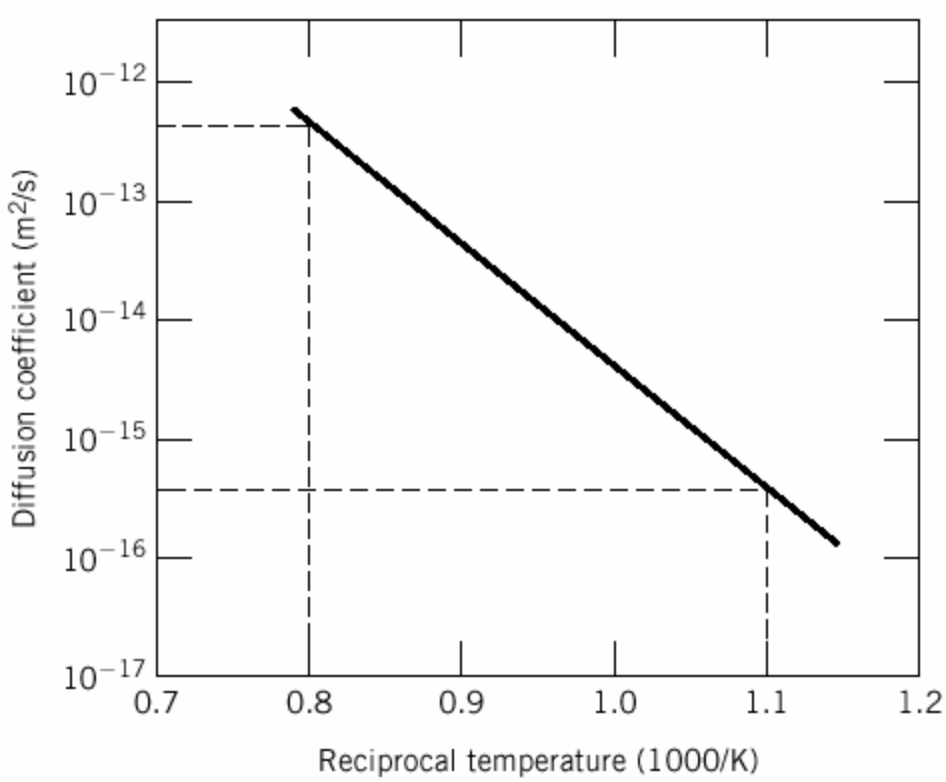

Figure 2.7: *A graph of lnD vs 1/T. Taken from reference [2].*

The equation of the line in the Figure.2.7 is given by, $y = ax + b$, where $x = \frac{1}{T}$, $a = -\frac{E_a}{k_B}$ and $b = \ln D_0$. This graph has a slope *a* and intercept of *b*.

Using equation 2.6, the diffusion coefficients of Eu in 6H-SiC was estimated at 1200 °C and 1300 °C respectively. The values of activation energy E_a and the pre-exponential D_0 were also deduced. The results are reported in chapter 5.

References

[1] Energy Models. (1981). *Basic Photovoltaic Principles and Methods*. [online] Available at: http://energy-models.com/basic-photovoltaic-principles-and-methods [Accessed 18 May 2016].

[2] people.virginia.edu. *Introduction to Materials Science*. [online] Available at: http://people.virginia.edu/~lz2n/mse209/Chapter5.pdf [Accessed 11 May 2016].

[3] Callister, W. and Rethwisch, D. (2011). *Materials Science and Engineering*. 8th ed. USA: John Wiley & Sons.

[4] www.eng.utah.edu. (2017). *Lecture 4: Diffusion: Fick's second law*. [online] Available at: http://www.eng.utah.edu/~lzang/images/lecture-4.pdf [Accessed 17 Jul. 2017].

[5] Google.co.za. (n.d.). *Google*. [online] Available at: https://www.google.co.za/?gws_rd=ssl#q=Chapter_7_Diffusion_in_Solids &*&spf=1 [Accessed 20 Jun. 2016].

[6] Anon, (n.d.). [online] Available at: http://personal.cityu.edu.hk/~appkchu/AP4120/8.PDF [Accessed 3 Oct. 2016].

[7] Dwaraknath, S.S. and Was, G.S. (2016). The diffusion of cesium, strontium, and europium in silicon carbide. *Journal of Nuclear Materials*, 476, pp.155-167.

[8] Anon, (2017). [online] Available at: http://www.its.caltech.edu/~ch24/lecture2.PDF [Accessed 12 Jan. 2017].

[9] Csik, A., Langer, G.A., Erdélyi, G., Beke, D.L., Erdelyi, Z. and Vad, K. (2008). Investigation of Sb diffusion in amorphous silicon. *Vacuum*, 82(2), pp.257- 260.

Chapter 3

ION IMPLANTATION

Ion implantation is a process whereby an energetic ion impinging a particular material (6H-SiC in this study) loses all of its energy until it comes to rest within material. In this study, Eu ions of energy 360 keV were implanted into single crystalline 6H-SiC at 600 ^{o}C. This chapter discusses the processes taking place during ion implantation until ions comes to rest inside material.

3.1. Ion interaction

During ion implantation an ion of a particular energy is accelerated towards a substrate/material of interest, where it interacts with the substrate atoms until it comes to rest. This process is mostly used to create semiconductors of n-type or p-type according to the ideal properties of the semiconductor [1]. Doping or implanting can make a non-conductive material to become conductive. Ion implantation can also be used to introduce a certain amount of ionized atoms in a certain crystal material for a specific purpose. In this study Eu^{+} ions were implanted into 6H-SiC to investigate the migration behaviour of Eu in 6H-SiC.

During ion implantation, ions interact with electrons and atoms of the target material resulting in scattering events (a process whereby atoms, electrons and the incident ions are forced to deviate from a straight trajectory due to localized non-uniformity in the medium through which they pass). These interactions slows down the projectile ions, reducing their energy until they come to rest. Depending on the projectile ion energy, the ion will eventually come to rest somewhere beyond the surface layers due to loss of its energy throughout the trajectory. For example, the use of 3 to 500 keV energy for boron, phosphorus or arsenic dopant ions is sufficient to implant the ions from 100 to 10000Å below the silicon surface [2, 3].

3.2. Radiation Damage

A continuous transfer of energy by the projectile or moving ion to the target atoms destroys atomic arrangement resulting in a damaged crystal lattice. Some of the ions that are penetrating through the lattice, interact with the lattice atoms displacing them from their original positions. The minimum energy that is required to knock off a lattice atom from its position is termed the displacement energy (E_d). If the energy E of the projectile ion is greater

than the displacement energy, the lattice atom that is involved in such a collision may be knocked out of its position. If the energy of the projectile ion is still larger than E_d after that collision, the ion may continue to knock out many other atoms until its energy is reduced to lower than E_d. Similarly if the initially knocked out atom has the energy larger than the E_d it will knock out other atoms giving them initial energy to collide with many other atoms. This process continues until the colliding atom/projectile loses all of its energy and come to rest in the lattice.

The number of displaced atoms caused by a projectile ion can be estimated by [4]:

$$N(E) = \frac{E_n}{2E_d} \tag{3.1}$$

where E_n is the energy lost in a collision and E_d *is* as described before.

The damage distribution in the lattice structure is different for heavy ions and for light ions. Below is the illustration of both light ion and heavy ion damage.

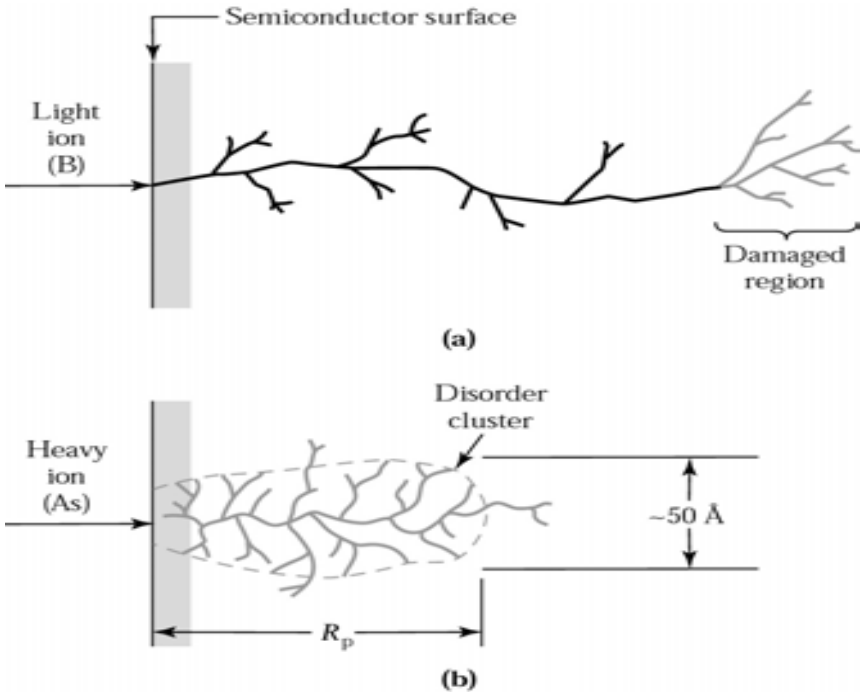

Figure 3.1: *Representation of damage distribution for heavy ions and light ions. Taken from reference [4].*

Heavy ion bombardment results in a high damage density over a small volume while light ions results in low damage density over large area. This is due to the fact that heavy ions are slow while light ions are faster ($v \propto M^{-\frac{1}{2}}$), hence, a fast particle has less interaction time with the scattering nucleus.

3.3. Energy loss

The knowledge of the slowing down of ions traversing matter is of fundamental importance in ion beam analysis of material. Depth scales follows directly from the energy lost by the probing particles and the energy loss affects both quantitative and compositional analysis. The definition of the concepts of energy loss, stopping cross section and stopping power varies in the literature. In this study, the energy loss per unit length, dE/dx is defined as

$$\lim_{\Delta x \to 0} \Delta E/\Delta x \equiv dE/dx(E) \tag{3.2}$$

Here ΔE is the amount of energy lost per distance Δx traversed. The relative importance of the various interaction processes between the ion and the target medium depend mostly on the ion energy/velocity and on the charge state of the ion and target atoms. As the ion velocity is increased the nuclear energy loss diminishes like $1/E$, where E is the (instantaneous) energy of the ion in the solid. The electronic energy loss, i.e. inelastic collisions with the atomic electrons, is usually the main mechanism by which ions lose their energy. The total energy loss is obtained as a sum of the nuclear and electronic contributions.

3.4. Ion Stopping

As highlighted earlier, an energetic ions penetrating material, interact with the atoms of material resulting in a number of collisions between ions and host atoms. These collisions reduce energy of the ions and finally stop them in the lattice. The ions lose their energy via two mechanisms i.e., Electronic stopping and nuclear stopping. Therefore, the total energy loss of the ions is the contribution of the two stopping:

$$\varepsilon = \varepsilon_e + \varepsilon_n \tag{3.3}$$

where ε_e and ε_n is electronic and nuclear stopping respectively. Figure.3.2 shows the contributions from nuclear and electronic stopping. The region to the far left of the Figure with low energy ions is dominated by nuclear stopping. The region in the middle with

intermediate energies immediately after the critical energy E_c is dominated by both electronic and nuclear stopping. The electronic stopping reaches its maximum and we enter the region of even higher energies called Bethe-Bloch region where only electronic stopping dominates.

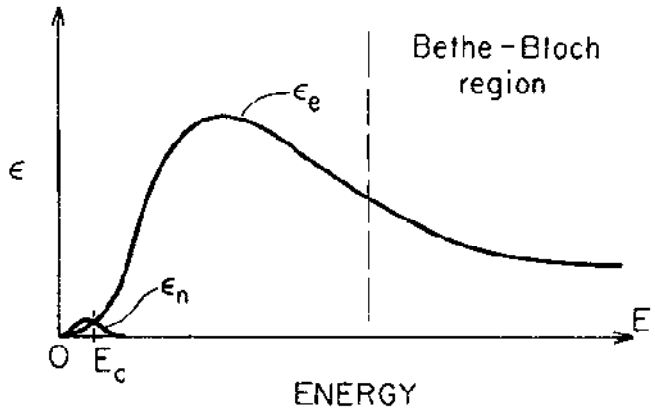

Figure 3.2: *A representation of the contribution of electronic stopping ε_e and nuclear stopping ε_n to the stopping cross section ε as a function of incident energy. Taken from reference [5].*

The stopping power S (which is equivalent to energy loss per unit length) of the ion path is given as:

$$S = -\frac{dE}{dx} = -\left[\left(\frac{dE}{dx}\right)_{nuclear} + \left(\frac{dE}{dx}\right)_{electronic}\right] = S_n + S_e \qquad (3.4)$$

where S_n and S_e are the nuclear stopping and electronic stopping factors respectively.

It is very important to determine the average energy loss by incident particles traversing a crystal. This can be achieved by first determining the cross section, i.e. the area that is impinged by a beam of particles on a sample. It quantifies the likelihood of scattering event when an incident beam strikes a target made up of discrete particles [6].

3.4.1. Nuclear Stopping

Nuclear energy loss dominates at lower energies, a region where the ion velocity is less than $v_0 Z^{2/3}$, where v_0 is the Bohr velocity given by $v_0 = e^2/\hbar$, e and $\hbar$ are electron charge and Planck's constant respectively, and Z is the ion atomic number (see Figure 3.2). In this region

the ion does not have enough energy to give to electrons that have energy lower than the Fermi level. During this process ions collide with target atoms, the positively charged ions are repelled by positive cores of the substrate lattice atoms.

Figure 3.3. shows an incident ion with m_1 interacting with nucleus with m_2 of a stationary atom. An angle θ depends on masses m_1, m_2 and on b (impact parameter), and maximum energy is transferred when $b = 0$.

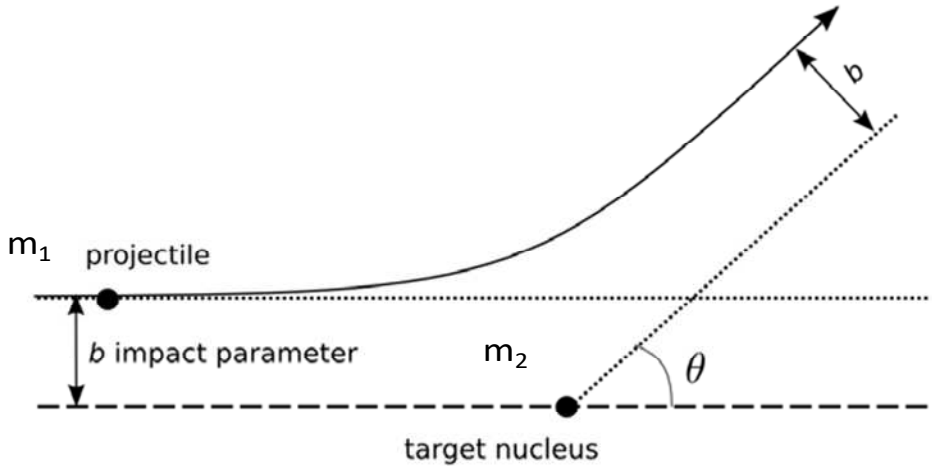

Figure 3.3: *Schematic of a nuclear scattering between an ion of energy E_1, mass m_1 and a stationary target atom of mass m_2; b is the impact parameter. Taken from reference [7].*

A collision between two charged particles or nuclear stopping can be described mathematically as follows: If one assumes an inelastic collision between an ion of mass m_1 (with an incident energy E_0) and a stationary atom of mass m_2 (which is initially stationary), the conservation of energy and momentum can be used to determine the energy transferred from the projectile to the stationary atom. The energy transferred to the atom is dependent on the scattering angle θ. Conservation of energy and momentum in the center of mass frame give the energy transferred T as [6]:

$$T = \frac{4E_0 m_1 m_2}{(m_1 + m_2)^2} \sin^2 \frac{\theta}{2} = T_{\max} \sin^2 \frac{\theta}{2} \qquad (3.5)$$

From equation 3.5, it is quite clear that during a head-on collision, i.e. $\theta=\pi$, a total energy (maximum energy) is transferred to the target atom. In case of a spherically symmetric potential, the scattering integral can be written as:

$$\theta = \pi - 2b\int_{r_{\min}}^{\infty} \frac{dr}{r^2\left[1-\frac{V(r)}{E_c}-\frac{b^2}{r^2}\right]} \tag{3.6}$$

E_c is the energy at the center of mass of the two interacting atoms, r is the polar coordinate from the projectile to atom. The two equations above give the relationship between θ, T and b from which the differential cross section can be calculated:

$$\sigma(E,T)dT = 2\pi b dT \tag{3.7}$$

$$\sigma(E,T) = 2\pi b\frac{db}{d\theta}\frac{d\theta}{dT} \tag{3.8}$$

$$\sigma(E,T) = \int \sigma(E,T)dT \tag{3.9}$$

These relations help us to determine the stopping power in equation 3.4.

In determining the stopping power, the repulsive potential acting between toms has to be first determined. It is rather a challenging task to find directly a repulsive potential. Several studies has measured the scattering cross sections of several ions in noble-gas targets [7]. Using Hartree-Fock and density-functional theory [7], interatomic potential $V(r)$ has been derived as:

$$V(r) = \frac{Z_1 Z_2 e^2}{r}\Phi(r) \tag{3.10}$$

where Z_1 and Z_2 are nuclear charges of the projectile ion and target atom respectively, r is the inter-nuclear distance between the target and bombarding nuclei. And $\Phi(r)$ is called a screening function.

There are several screening functions. The one by M Backman [7] and is given as:

$$\Phi(x) = 0.1818e^{-3.2x}+0.5099e^{-0.9423x}+0.2802e^{-0.4029x}+0.02817e^{-0.2016x} \tag{3.11}$$

In this equation r is substituted by x.

Stopping power can be obtained from the universal interatomic potential (equation 3.10)and differential cross section (equations 3.7 to 3.9).

3.4.2. Electronic Stopping

When ions with high energies (velocity greater than $v_0 Z^{2/3}$) penetrate a material, they experience a drag due to free electrons. These "free" electrons exist because a large space in a crystal is composed of the electron clouds of the atoms. When an ion passes through an electron cloud, it attracts the electrons and causes internal electronic transitions. The drag force is exerted on a moving ion in an electron cloud, ion moves in the same direction. An example of an ion entering and exiting electron cloud is shown in Figure 3.4,

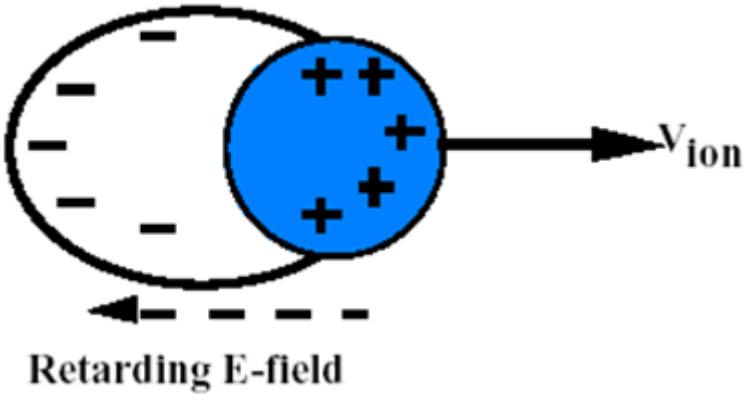

Figure 3.4: *Electronic transition caused by an ion passing electron cloud. Taken from reference [4].*

Electronic energy loss dominates at higher ion velocities (about $10^5 m/s$ and higher). At these high velocities the ion is stripped of its electrons. Coulomb scattering is observed between the ions and electrons, thus the stopping power is extracted from the scattering integral using NZ_2 as the electron density and excluding screening function:

$$\left(\frac{dE}{dx}\right)_e = 8\sigma_e N\left(\frac{m_e}{m_1}\right)^{1/2} E^{1/2} = kE^{1/2} \qquad (3.12)$$

where k is $8\sigma_e N\left(\frac{m_e}{m_1}\right)^{1/2}$. This equation gives a good approximation of electronic stopping power [7].

In the region where electronic stopping reaches maximum, the ion is partly ionized and has a velocity approximately equal to the Bohr velocity (see figure 3.2).

At higher energies, the velocity of the ion is much greater than the Bohr velocity and thus the ion is stripped of all its electrons. This region is

known as Bethe-Bloch who found that the energy loss in this region is proportional to Z_1^2, where Z_1 is the atomic number of the ion [8]. Electronic stopping in this region is given by Bethe-Bloch equation [8, 9]:

$$\varepsilon_e = \frac{4\pi Z_1^2 Z_2 e^4}{m_e v_1^2}\left[\ln\left(\frac{2m_e v_1^2}{I}\right) + \ln\left(\frac{1}{1-\beta^2}\right) - \beta^2 - \frac{C}{Z_2}\right] \tag{3.13}$$

where m_e is the electron mass, v_1 is the velocity of the projectile, $\beta = v/c$ where c is the speed of light, I is the average ionisation potential and c/Z_2 is the shell correction.

3.5. Range and Range Straggling

Range along the ion path is the total distance that the ion traversed along the trajectory within the substrate/target [10]. The range calculation using equation 3.14, which involves the contributions from both ion stopping mechanisms (electronic and nuclear stopping) is given as:

$$R = \int_0^R dx = \frac{1}{N}\int_0^{E_0} \frac{dE}{S_n(E) + S_e(E)} \tag{3.14}$$

where N is the number of atoms per volume unit, E_0 is the projectile initial energy and S_n and S_e are the nuclear and electronic stopping respectively.

The average depth of the implanted ions is called the projected range (R_p), and can be estimated by the position of the peak height of the Gaussian distribution of the implanted profile. The standard deviation of the Gaussian distribution gives the so called "range straggle" ΔR_p.

Figure 3.5 illustrates an ion penetrating a substrate and finally coming to stop at projected rangeR_p.

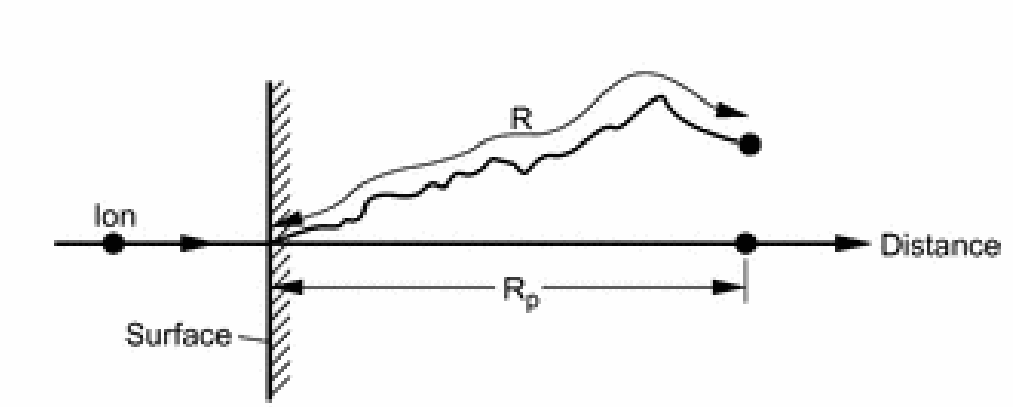

Figure 3.5: *An ion incident on a semiconductor penetrate with a total path length R giving a projected range R_p. Taken from reference [11].*

A Gaussian distribution of Eu ions(360 keV) implanted into 6H-SiC indicating the projected range and the range struggle is shown in Figure 3.6.

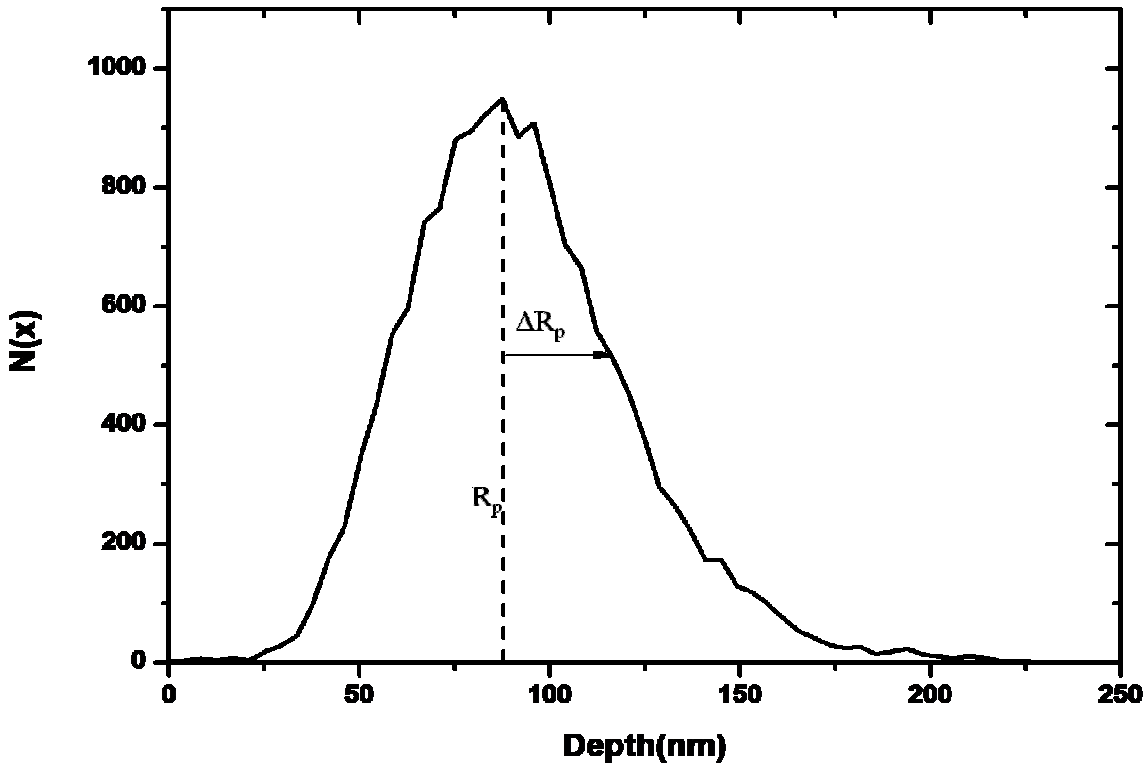

Figure 3.6: *Range distributions for Eu ion implanted into 6H-SiC. N(x) is the number of ions and the depth represents the distance into the solid. The projected range is also indicated in the figure.*

3.6. Simulation of ion implantation

A simulation of ions implanted into a certain material is necessary in predicting the shape and depth of the expected spectrum. This simulation help us choose energies for implantations at desired depths. A Monte Carlo computer program is used to calculate the range distributions of a variety of ion/target combinations. In this study a TRIM program was used to simulate implantation of 360 *keV* europium ions into 6H-SiC. When performing the calculations, TRIM assumes the following:

- That the interaction of ion and target is a binary collision, ignoring the influence of the surrounding atoms.
- Recombination of atoms with vacancies is neglected.
- The interatomic potential as a universal form which is an averaging fit to quantum mechanical calculations using experimental data.

Even with these assumptions in place, TRIM still maintains moderate accuracy with a percent error of about 5-10%. Figure. 3.7 shows the TRIM results of a 360 keV Eu ions implanted in 6H-SiC, experimental results are included for comparison.

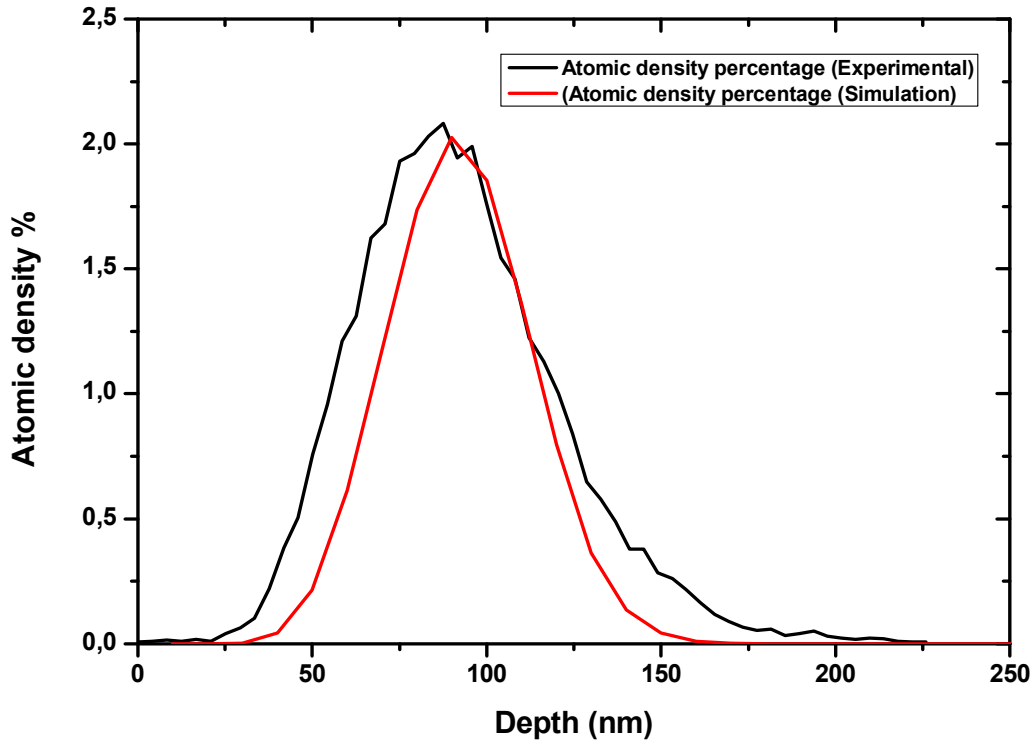

Figure 3.7: *A TRIM simulation of 360 keV Eu ions implanted in 6H-SiC, with an experimental profile is shown (black) for comparison.*

References

[1] Rubin, L. and Poate, J. (2003). Ion Implantation in Silicon Technology. *American Institute of Physics*. [online] Available at: http://www.axcelis.com/sites/default/files/docs/Ion_Implantation_in_Silicon_Technology.pdf [Accessed 27 Oct. 2016].

[2] personal.cityu.edu. *Ion Implatation*. [online] Available at: http://personal.cityu.edu.hk/~appkchu/AP4120/9.PDF [Accessed 3 Oct. 2016].

[3] Dileepnanotech.com. *Micro and Nanofabrication of Gold Structures on Silicon Substrate*. [online] Available at: http://www.dileepnanotech.com/articles/Lithography.html [Accessed 23 Aug. 2016].

[4] Scribd. *Chapter 8 Ion Implantation _ II*. [online] Available at: https://www.scribd.com/presentation/236706280/Chapter-8-Ion- Implantation-II [Accessed 26 Jul. 2016].

[5] Chu, W., Mayer, J.W. and Nicolet, M.A. (1978). *Backscattering spectrometry*. 1st ed. New York: Academic Press.

[6] Mohammad, E.J., Hazem, R.S. and Mohammed, A.J. (2017). Silicon Photon Absorber (Photon Cross Section). *International Journal of Science and Engineering Investigations*, 6(60).

[7] Backman, M. (2012). *Effects of nuclear and electronic stopping power on ion irradiation of silicon-based compounds*. MSc. University of Helsinki.

[8] Andersen, H. and Ziegler, J. (1977). *Hydrogen*. 1st ed. New York: Pergamon.

[9] Leung, P.T. (1989). Bethe stopping-power theory for heavy-target atoms. *Physical Review A*, 40(9), pp.5417-5419.

[10] Tesma, J.R and Nastasi, M. (1995). *Handbook of Modern Ion Beam Materials Analysis*. 1st ed. Pennsylvania: Materials Research Society, pp.15-16.

[11] Nastasi, M. and Mayer, J.W. (2006). *Ion Implantation and Synthesis of Materials*. 1st ed. Berlin: Spinger, pp.63-76.

[12] Globalspec.com. (2006). *Chapter 8: Channeling | Engineering360*. [online] Available at: http://www.globalspec.com/reference/66957/203279/chapter-8-channeling [Accessed 12 Mar. 2017].

[13] personal.cityu.edu. (n.d.). [online] Available at: http://personal.cityu.edu.hk/~appkchu/AP4120/9.PDF [Accessed 16 Nov. 2016].

[14] Narayan, J., Oen, O.S., Fathy, D. and Holland, O.W. (1985). Atomic Structure of Collision Cascades in Ion-Implanted Silicon and Channeling Effects. *Elsevier Science Publishers*.

[15] Weinberger, P. (2014). Niels Bohr and the dawn of quantum theory. *Philosophical Magazine*, 94(27), pp.3072-3087.

[16] Randall, L. (n.d.). [online] web.mit.edu. Available at: http://web.mit.edu/8.01t/www/materials/modules/chapter15.pdf [Accessed 10 Aug. 2016].

[17] Doolittle, A. (n.d.). *Ion Implantation*. [online] alan.ece.gatech.edu. Available at: http://alan.ece.gatech.edu/ECE6450/Lectures/ECE6450L5- Ion%20Implantation.pdf [Accessed 3 Oct. 2016].

[18] Cesini, G., Lucarni, G. and Rustichelli, F. (1975). Evaluation of fission fragment ranges in any medium. *Nuclear Instruments and Methods*, [online] 127(4), pp.579-582. Available at: http://www.sciencedirect.com/science/article/pii/0029554X75906618 [Accessed 1 Aug. 2016].

[19] Kachurin, G.A., Tyschenko, I.E. and Fedina, L.I (1992). High-temperature ion implantation in silicon. *Nuclear Instruments and Methods in Physics Research*, B68, pp.323-330.

[20] Fuller, L., Turkman, R. and Pearson, R. (2013). *INTRODUCTION TO ION IMPLANTATION*.

[21] Hickey, D.P. (2007). *Ion Implantation Induced Defect Formation And Amorphization In The Group iv Semiconductors: Silicon And Diamond, Germanium*. MSc. University Of Florida.

[22] Chason, E., Picraux, S.T., Poate, J.M., Borland, J.O., Current, M.I., Diaz de la Rubia, T., Eaglesham, D.J., Holland, O.W., Law, M.E., Magee, C.W., Mayer, J.W., Melngailis, J. and Tasch, A.F. (1997). Ion beams in silicon processing and characterization. *Journal of Applied Physics*, 81(10), pp.6513-6561.

[23] Giannuzzi, L.A., Kempshall, B.W. and Prenitzer, B.I. (2004). Ion-Solid Interaction. In: L. Giannuzzi, ed., *Introduction to Focused Ion Beams*, 1st ed. New York: Springer.

Chapter 4

EXPERIMENTAL TECHNIQUES

In this study Rutherford backscattering spectrometry (RBS) and scanning electron microscopy (SEM) were used to investigate the migration behaviour of Eu ions implanted into single crystalline 6H-SiC. This chapter discusses the experimental techniques used in this study.

4.1. Rutherford Backscattering Spectrometry (RBS)

Rutherford Backscattering Spectrometry (RBS) is an analytical technique used in materials science to determine the structure and composition of materials by measuring the backscattered beam of energetic ions impinging on material. RBS consists of five parts namely, the accelerator/Van De Graaff Generator, the beam line, analysis chamber, the detector and the data acquisition set-up. They are discussed in detail below.

4.1.1. The Van De Graaff Generator

In this study, positive helium ions (He^{+}) that are used to analyze 6H-SiC implanted with Eu ions were produced by an ion source and accelerated by a Van De Graaff accelerator to an energy of 1.4 and 1.6 MeV.

The helium (He) gas was ionized by a radio-frequency (rf) signal. The ionized gas resulted in a He gas plasma. A positive potential was then applied to the anode. Positive ions from the plasma are then repelled through the exit of the bottle into the acceleration path of the accelerator. A typical rf ion source with electrodes and exit channel is shown in Figure 4.1:

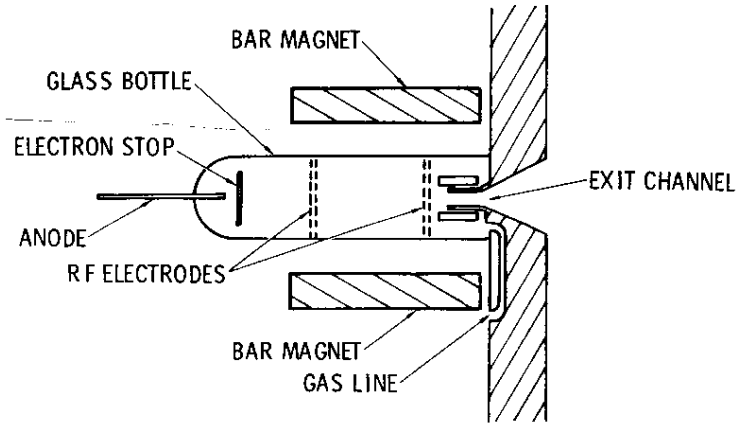

Figure 4.1: *Schematic representation of an rf ion source. Taken from reference [1].*

In a Van De Graaff generator, a pulley drives an insulating belt by a sharply pointed metal comb which has been given a positive charge (charging screen) by a power supply [2]. Positive ions are removed from the belt by another comb at the top (collection screen). This allows the net positive charge to spread onto the terminal shell. Thus the belt accumulates electric charge on the terminal shell producing high voltage on the terminal shell. This high potential is used to further accelerate the positive ions (He^{+}) along the beam line. Figure 4.2 shows a typical schematic of a Van De Graaff accelerator.

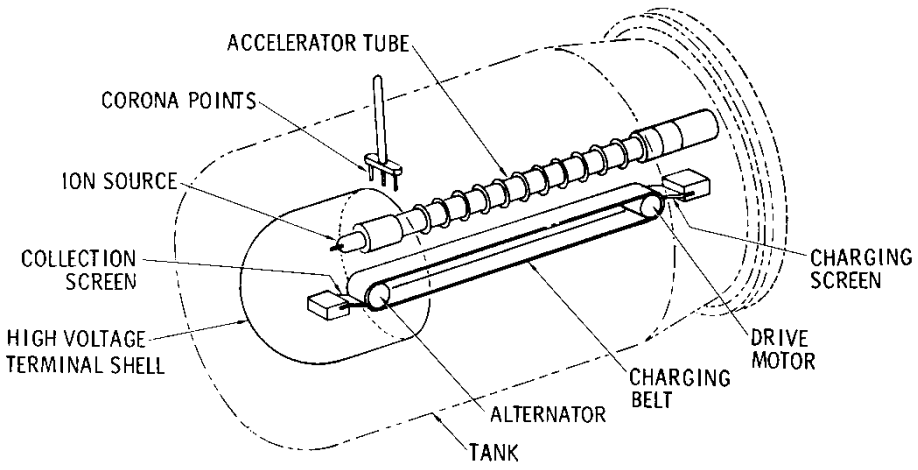

Figure 4.2: *Schematic diagram of a Van De Graaff accelerator. Taken from reference [1].*

To minimize collisions between the accelerated ions and the molecules in the acceleration tube, the tube is highly evacuated to normal operating pressures of 10^{-6} mbar. For the accelerator employed at UP, the tube pressure is kept at about 10^{-8} mbar. If the pressure in the tube goes up to about 10^{-4} mbar, a voltage breakdown can occur.

The terminal shell and the accelerating tube are covered by a tank. The tank is normally filled with dry gases such as N_2, CO_2, or SF_6 to prevent sparking of the high voltage to the terminal which is at ground potential [1]. The tank is first evacuated before filling it with the gases. In our case a mixture of N_2 and CO_2 was used.

4.1.2. The beam-line

A beam of high-energy ions is accelerated to the target along a drift tube/beam-line that is maintained at low pressures. A vacuum between 10^{-5} mbar and 10^{-7} mbar is sufficient for minimum collision probability between ions and residual gas molecules. The UP accelerator beam-line is kept at 10^{-9} mbar of pressure. The beam must have a uniform distribution along the appropriately shaped cross section for the analysis of the sample. The shape of the beam cross section is defined by collimators. They are typically circular holes of diameter ranging from less than 1mm up to 1cm. A 1 mm collimator was used in this study.

4.1.3. Target and analysis chamber

The target is positioned in a chamber where it interacts with the beam. In the same way as the accelerator tube and the beam-line, the chamber is also evacuated to lower pressures. A mechanical pump is used to evacuate the chamber to reduce the pressure to the moderate pressures of 10^{-2} mbar, the starting pressure for the turbo-molecular pump. At this pressure, a turbo pump is employed to pump down to lower pressures of about 10^{-6} mbar. After analysis the chamber is vented with air to the atmospheric pressure.

The beam current is measured directly at the sample. The secondary electrons (from the interactions of the beam with the target) which may falsify the current measurement are suppressed by applying negative suppression voltage of approximately -100 V on the suppressor plates (located in front of the target).

A controlled ion beam bombards the sample placed in a sample holder at a certain angle (ion incident angle), 0^o in this project. The backscattered ions are detected by a detector located at a certain angle (scattering angle) with respect to the incident angle. The scattering angle used in this project was 165^o.

4.1.4. The detector and data acquisition

The RBS at the University of Pretoria employs a Si-surface-barrier-solid state detector for the detection of backscattered energetic ions. A typical solid-state detector is shown in Figure 4.3.

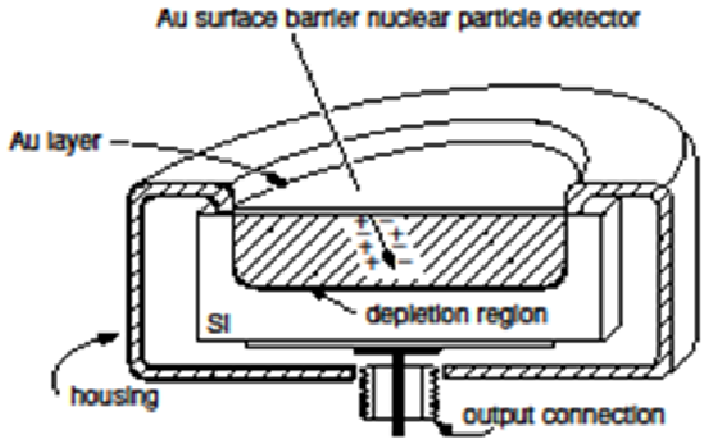

Figure 4.3: *Schematic representation of a gold-surface barrier nuclear particle detector. Taken from reference [3].*

When a backscattered energetic ion passed through the depletion region, electrons-holes are created. The number of electrons-holes is proportional to the energy of the backscattered particle. The electrons-holes are detected by applying the biased voltage of about 40 V to the detector. The detector is connected to a preamplifier which generates a pulse for each incident ion. The height of the pulse is proportional to the energy of the detected particle. The generated pulse is then fed into the amplifier where it is amplified. The amplified analogy signal is fed into a multichannel analyser (MCA) where it is digitalized [4]. The digitized data is then displayed on a computer screen in XY plane of Counts and channel number where the counts and channel number are equivalent to concentration and backscattered energy respectively. A typical RBS spectrum of 6H-SiC implanted with Eu is shown in Figure 4.4, the surface positions of elements are indicated by arrows:

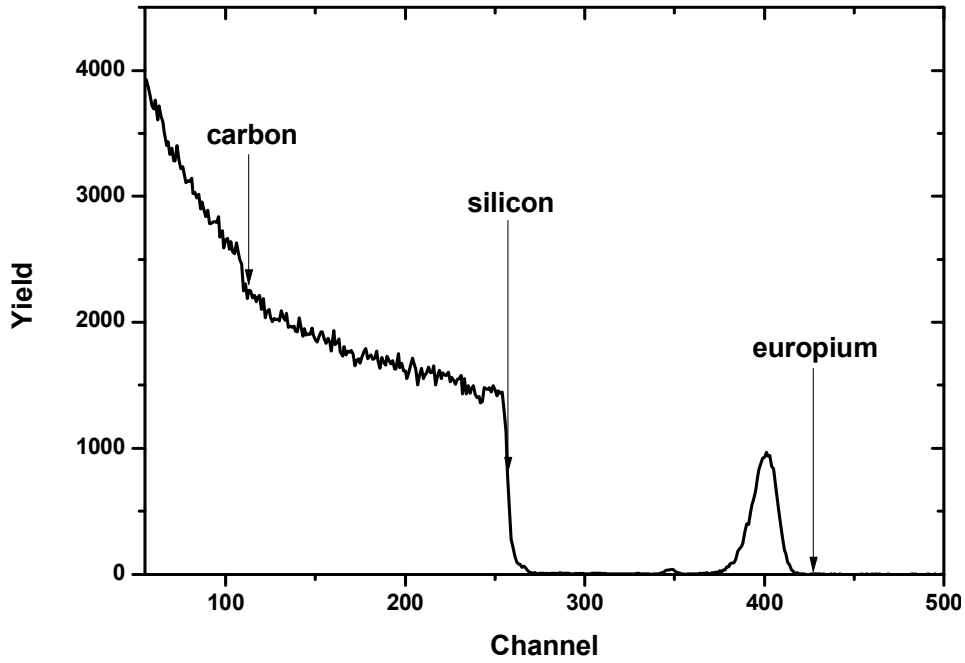

Figure 4.4: *A typical RBS spectrum of 6H-SiC implanted with Eu, arrows indicate surface positions of elements.*

4.2.The kinematic factor

During RBS analysis, a target is bombarded with particles (M_1) of a given initial energy (E_0) and velocity v_0. These particles collide with a stationary target (M_2) which then recoils with energy E_2 and velocity v_2. The projectile backscatters with energy E_1.as shown in Figure 4.5.

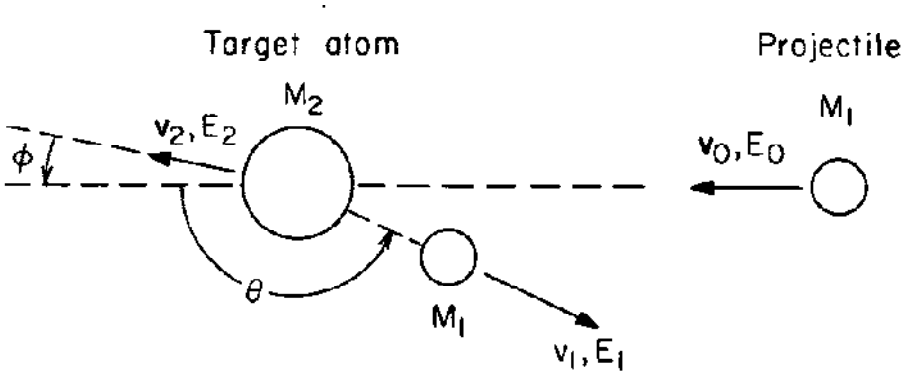

Figure 4.5: *A schematic representation of a elastic collision of a projectile of mass M_1, velocity v_0, incident energy E_0 and a stationary target atom of mass M_2. After the collision the projectile has energy E_1, and velocity v_1, the target atom has energy E_2 and velocity v_2. θ is a backscattering angle. Taken from reference [1].*

Applying the principles of conservation of energy and momentum, the energy of backscattered particle E_1 can be found [1]. The ratio of the projectile energy before collision to that of the projectile after collision (backscattered particle) is called the kinematic factor K:

$$E_1 = KE_0 \tag{4.1}$$

Using conservation of energy and momentum, K is found to be [1]:

$$K = \frac{m_1^2}{(m_1 + m_2)^2}\left\{\cos\theta \pm \left[\left(\frac{m_2}{m_1}\right)^2 - \sin^2\theta\right]^{1/2}\right\}^2 \tag{4.2}$$

The energy E_1 of the particles backscattered from known surface elements can be calculated using equation. 4.1. If $m_1 < m_2$ only the positive sign is used in equation. 4.2. If $m_1 > m_2$ then equation. 4.2. has two solutions, and the maximum possible scattering angle θ_{max} is given by [5]:

$$\theta_{\max} = \arcsin\left(\frac{m_2}{m_1}\right) \tag{4.3}$$

In this project $m_1 < m_2$.

4.3.Depth Scaling

Not all incident energetic particles are backscattered from the surface. Some of the incident particles penetrate the sample, and their energy is lost as a result of interactions between the particles and the various atomic elements composing in the target material. Some of the penetrating ions backscatters inside the material/sample after losing some energy and they lose energy on their way back to the surface. A typical schematic diagram illustrating such a process is shown in Figure 4.6.

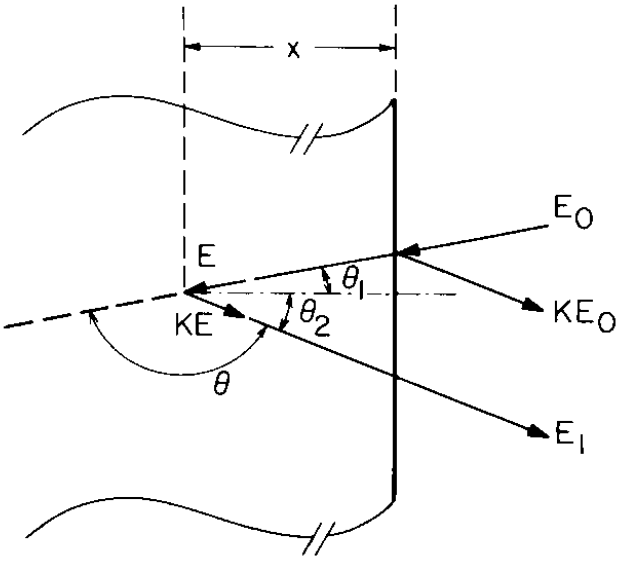

Figure 4.6: *A schematic representation of a backscattering event in a sample consisting of one element, bombarded with particles of energy E_0. Taken from reference [1].*

An energetic ion of initial E_0, backscatters on the surface with energy KE_o. The penetrating ion loses some of its energy before backscattering at depth x from the surface. The ion has energy E before backscattering at x and has energy KE after backscattering. The particle backscattered at x loses energy on its way out. E_1 is the energy of the particle emerging from the surface after backscattering at depth x. The scattering angle θ is given by $\theta=180^o- \theta_1- \theta_2$, where θ_1 and θ_2 are the angles between the sample normal and the direction of the incident beam and of the scattered particle, respectively.

The energy difference of a particle scattered at the surface and a particle scattered at depth x is denoted by:

$$\Delta E = KE_0 - E_1 \tag{4.4}$$

where $KE_0- E_1$ is given as a function of x by[1]:

$$\Delta E = KE_0 - E_1 = \left[\frac{K}{\cos\theta_1} \left.\frac{dE}{dx}\right|_{in} + \frac{1}{\cos\theta_2} \left.\frac{dE}{dx}\right|_{out} \right] x \tag{4.5}$$

$\left.\frac{dE}{dx}\right|_{in}$ and $\left.\frac{dE}{dx}\right|_{out}$ are the constant energy loss values along the inward and outward paths of the traversing ion. If factor in square brackets in equation 4.5 (the energy loss factor) is replaced by S. Thus equation 4.5 can be written as:

$$\Delta E = [S]x \tag{4.6}$$

In terms of stopping cross sections, equation 4.6 can be rewritten as:

$$\Delta E = [\varepsilon]Nx \tag{4.7}$$

For a single element material, ε is the stopping cross section factor given by:

$$[\varepsilon] = \left[\frac{K}{\cos\theta_1} \varepsilon_{in} + \frac{1}{\cos\theta_2} \varepsilon_{out} \right] \tag{4.8}$$

For a material consisting of more than one element i.e A_mB_n, a stopping cross section factor is given by Bragg's rule:

$$\varepsilon_{AB} = m\varepsilon_A + n\varepsilon_B \tag{4.9}$$

Consequently the total energy loss is given by

$$\Delta E_{AB} = \varepsilon_{AB} Nx \tag{4.10}$$

where N is the molar density.

4.4. Differential cross section

The likelihood of a backscattering event to occur can be explained by the idea of a differential cross section. For an elastic collision in the laboratory frame of reference, the probability of a backscattering to occur is given as [1]:

$$\frac{d\sigma}{d\Omega} = \left(\frac{Z_1 Z_2 e^2}{4E} \right)^2 \frac{4}{\sin^2\theta} \frac{\{[1-((m_1/m_2)\sin\theta)^2]^{1/2} + \cos\theta\}^2}{[1-((m_1/m_2)\sin\theta)^2]^{1/2}} \tag{4.11}$$

where Z_1 is the atomic number of the incident atom with mass m_1, z_2 is the atomic number of the target atom with mass m_2, e is the electronic charge and E is the energy of projectile ion. The direct proportionality of $d\sigma/d\Omega$ to Z_1 and Z_2 explains the higher sensitivity of the backscattering spectrometry to elements with bigger mass than for the ones with smaller mass. The inverse proportionality of $d\sigma/d\Omega$ to the square of the projectile energy E_2 explains the higher backscattering yield for low energy ions than for high energy ions.

The total number of detected particles can be written as:

$$A = \sigma \Omega Q N t \tag{4.12}$$

where Ω is a solid angle, Q is the total number of incident particles, Nt is the number of target atoms per unit area perpendicular to the beam and σ is the differential cross section. If σ and Ω are known, the number of atoms per unit area in the target can be determined.

4.5. Ion Channelling

Channelling is the steering of a beam of energetic ions into open spaces (channels) between close-packed rows or planes of atoms in a crystal (see figure 4.8). Channelling is being used to measure implantation damage, dislocation networks, quality of epitaxial layers and strain in strained layer super-lattices. This steering avoids close encounters with the atoms in the close-packed rows and planes as a result of which the yield of the backscattering spectrum decreases. In the presence of an interstitial atom or displaced host atoms in the row or the planes of the crystal, the channelled beam will be backscattered and the normalized yield will increase. In this study channelling was used to measure the radiation damage retained in 6H-SiC by Eu implantation and their annealing after heat treatment of the samples at various temperatures. The spectrum obtained by channelling of ions is termed the aligned spectra while the one obtained without aligning the beam of energetic ions is termed the random spectra. Channelling only occurs if the ion's incident angle is small. Consequently only those ions at the angle less than the critical angle φ_c experience channelling. The critical angle is given as:

$$\varphi_c = 9.73\sqrt{\frac{Z_1 Z_2}{Ed}} \tag{4.11}$$

Where Z_1 and Z_2 are the incident ion atomic number and target atom atomic number respectively. E is the projectile energy and d is the atomic spacing in a crystal.

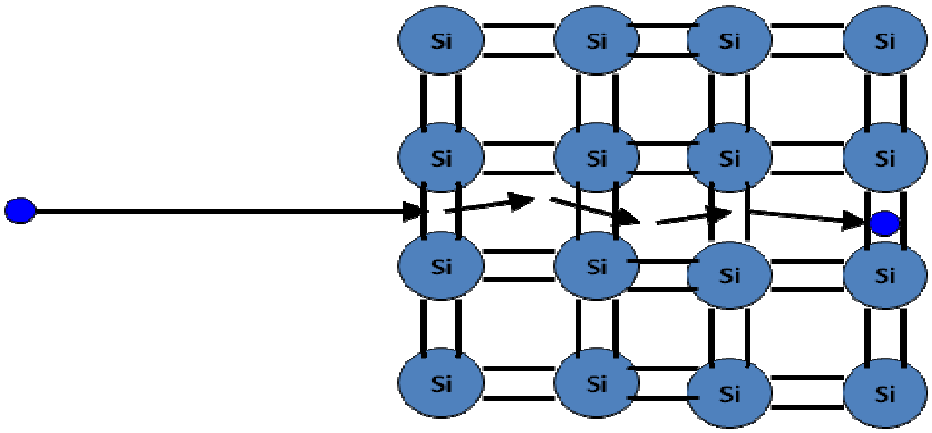

Figure 4.8: *Illustration of a channelling effect of an incident ion passing through atomic spacing of silicon crystal. Taken from reference [6].*

In (Fig.4.9), the random and aligned spectra is shown for an as-implanted 6H-SiC implanted with Eu ions at 360 keV ion energy at 600 °C.

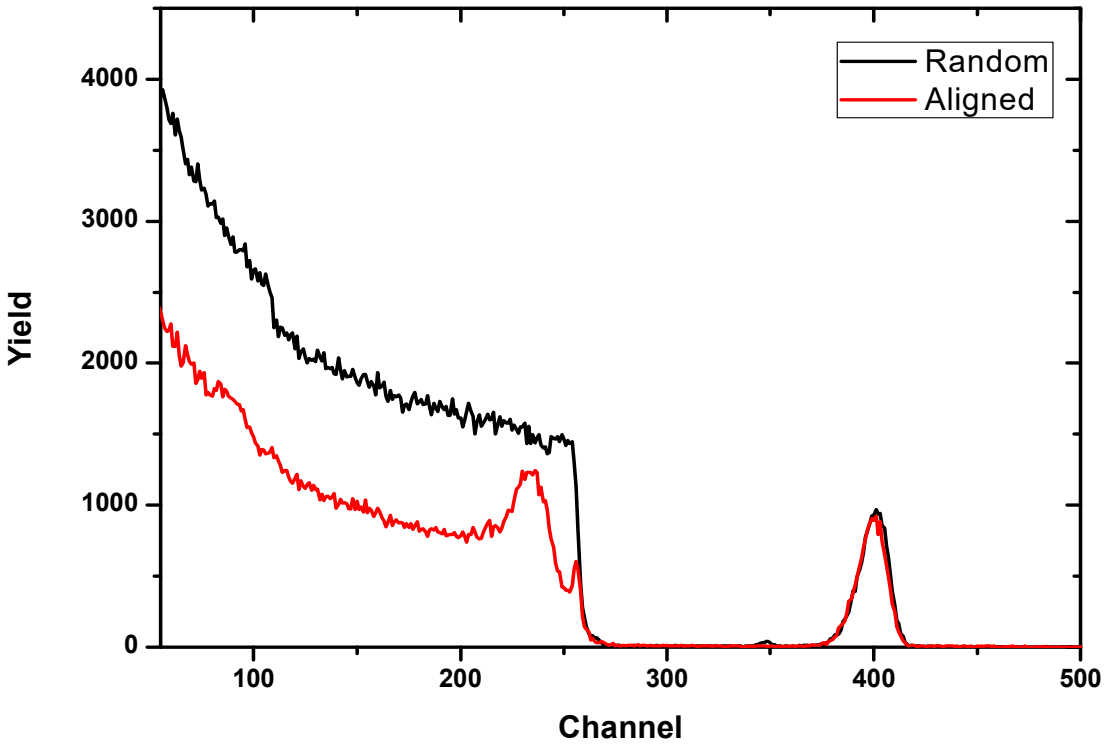

Figure 4.9: *A spectra of 360 KeV Eu ions implanted in 6H-SiC, a random spectrum and aligned spectrum are shown.*

In this study channelling was done by aligning the beam along the direction of the crystal using a three axis goniometer. For finding a channel in 6H-SiC, one axis (z-axis) was taken as

a reference, this axis is normal to the sample plane. The channel was searched by scanning the sample around the x-y plane perpendicular to the z-axis. This was done by scanning the sample first in the y-axis and then again in the x-axis in steps of 0.2˚. To avoid the surface backscattering, the energy window was set between the silicon surface energy and the carbon surface energy using the single channel analyser (SCA). The yield was recorded for both x- and y scans together with the corresponding angles. The minimum backscattered yield were chosen and plotted against the corresponding angles. This process was repeated while reducing the angular scan, and enough points were plotted until the directions of the formed planes were obtained. A channel is found at the point where any two planes intersect each other. After finding the channel, the energy window was set back to include the whole backscattered particles, and then a full spectrum is collected.

RBS-C was used in this study to monitor the retained damage in 6H-SiC after implantation and after every annealing of the sample. To avoid channeling while recording the random spectrum, the spectrum was collected 5˚ away from the channel. A comparison of a random and aligned spectra is shown in figure 4.9.

4.6. Scanning Electron Microscopy (SEM)

The changes in sample's surfaces after implantation and after annealing were monitored by scanning electron microscopy (SEM). SEM is an instrument used to generate images of specimen surfaces by scanning the sample with a beam of electrons in the x- and y-directions. Figure 4.10. shows the main components of a typical SEM.

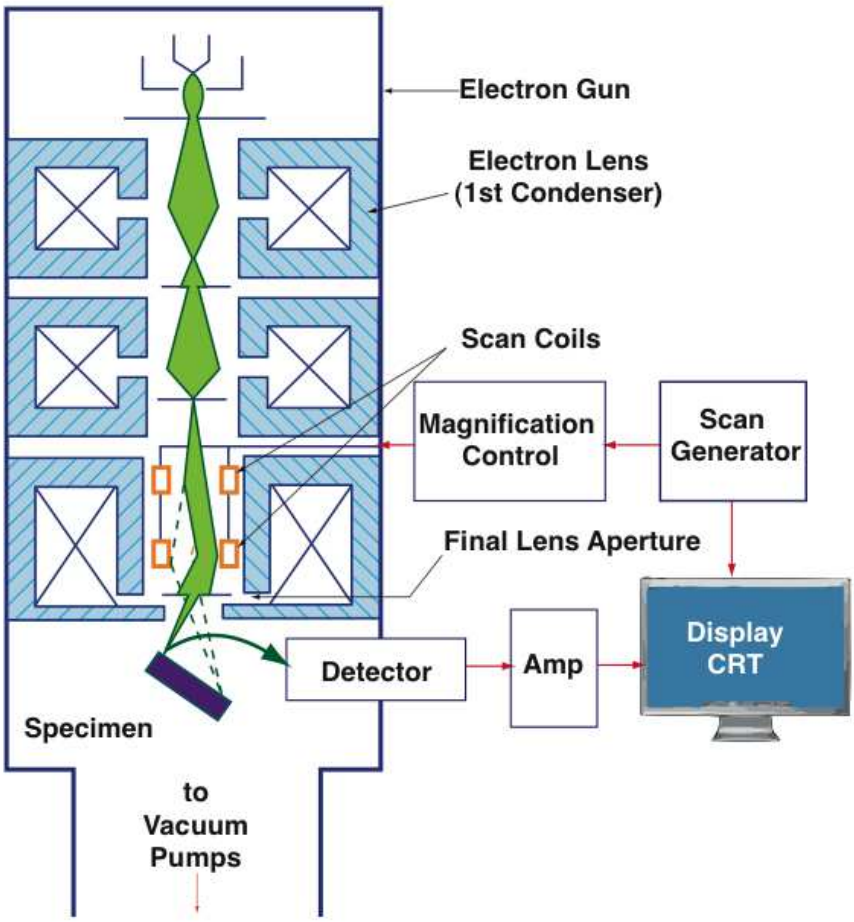

Figure 4.10: *Schematic representation of scanning electron microscopy. Taken from reference [7].*

The electron gun generates free electrons and accelerates them to energies in the 1-40 kV range. In this study an electron energy of 2 kV was used in all measurements. The electromagnetic lenses create a small focused electron probe on the sample. The scanning coils scan the electron beam across the surface of the sample and focuses it into a fine probe to produce images. The electron column operates in vacuum to allow the electron beam to travel freely thus minimizing interactions with the gaseous molecules that are present at high pressures.

When a sample is bombarded with electrons, signals are emitted in the form of electromagnetic radiation. These signals, mostly secondary electrons (SE) and backscattered electrons (BSE), are collected by detectors and amplified for final display on a computer monitor. Secondary electrons are low energy electrons with energy of approximately 5 eV [7]. BSE are high energy electrons with energies about the same as the energy of the incident beam. BSE and SE can be used for image formation. SE images

show mainly the topography of the sample surface. Auger electrons are ejected from atoms in response to a downward transition by an electron from higher energy state to lower energy state. The downward transition results in an emitted photon or an x-ray signal. These two signals can be used for chemical analyses of the sample (e.g. the composition of the sample, etc).

The function of electron lenses in SEM is to produce a uniform electron beam with desired diameter. The final lens aperture controls the aberrations and the resolution of the image. The detector detects the radiation signals that are emitted during electron beam interaction with the sample. Figure 4.11 shows the types of signals emitted during electron interaction with specimen in SEM:

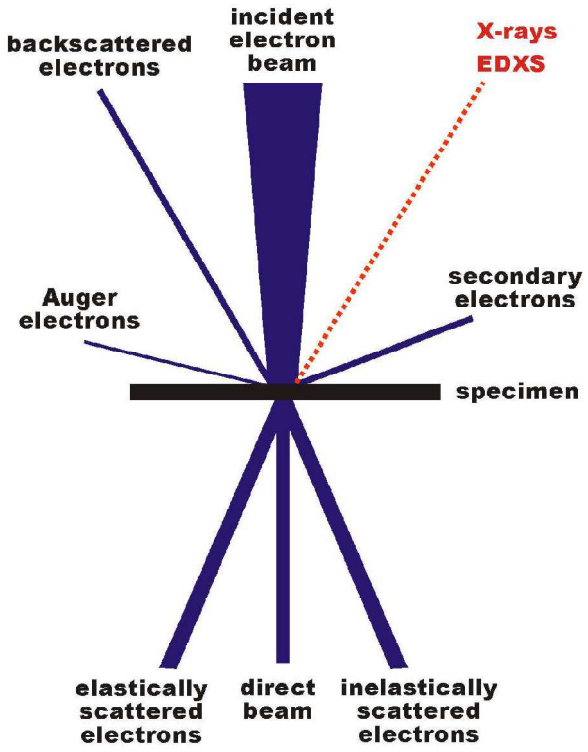

Figure 4.11: *Schematic of electron-matter interactions arising from the impact of an electron beam onto a sample. Taken from reference [8].*

In this study a field emission scanning electron microscope (FEG-SEM) was used. This microscopy employs Zeiss Ultra 55 instrument fitted with SE (secondary) detectors, BS (backscattered electron) detectors and an in-lens SE detectors. For the analyses of our samples, the in-lens SE detectors was used and the results are reported in chapter 6.

The image details and resolution in the SEM are determined by the size and characteristics of the interaction volume. The electron beam interacts and penetrate the sample to approximately 1 μm depth. The elastic and inelastic scattering controls the depth to which the electron beam penetrates in the solid. This forms an interaction volume from which different signals emerge. Figure 4.12. shows schematic of an interaction volume:

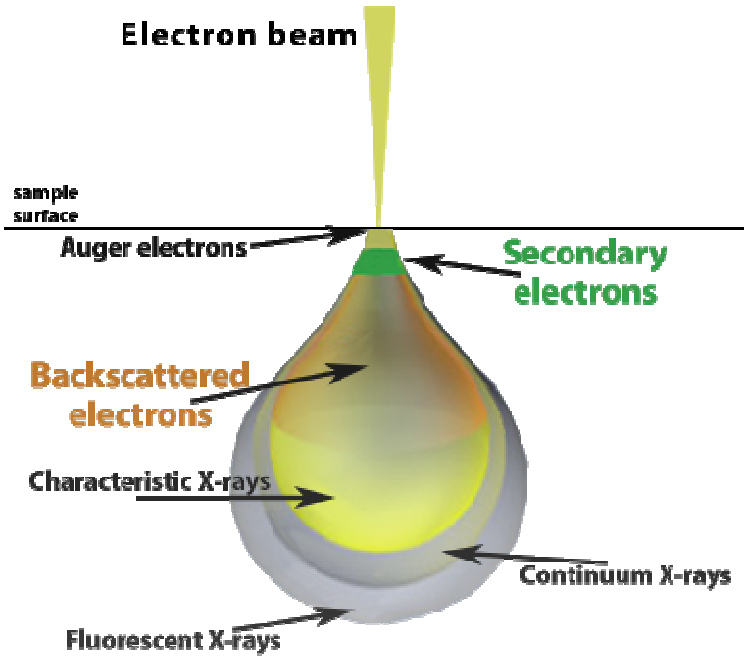

Figure 4.12: *A schematic diagram of a beam interaction with sample and the corresponding emitted signals at different depths. Taken from reference [9].*

The nature of imaging in SEM is determined by the interaction volume. The interaction volume increases with increasing beam energy and decreases with atomic number of the atoms in the sample.

Samples must be clean and compatible with high vacuum environment. This is especially necessary since SEM operates in high vacuum(~ 10^{-5}mbar).

Reference

[1] Chu, W., Mayer, J.W. and Nicolet, M.A. (1978). *Backscattering spectrometry*. 1st ed. New York: Academic Press.

[2] Hyperphysics.phy-astr.gsu.edu. (2017). *van de Graaff Generator*. [online] Available at: http://hyperphysics.phy-astr.gsu.edu/hbase/electric/vandeg.html [Accessed 27 Oct. 2015].

[3] Alford, T.L., Feldman, L.C. and Mayer, J.W. (2007). *Fundamentals of Nanoscale Film Analysis*. 1st ed. New York City: Springer, p.15.

[4] Pászti, F., Kótai, A. and Fazinic, S. (2000). Instrumentation For PIXE And RBS. *International Atomic Energy Agency*.

[5] Mayer, M. (2003). *Rutherford Backscattering Spectrometry (RBS).*

[6] Scribd. (2017). *Chapter 8 Ion Implantation _ II*. [online] Available at: https://www.scribd.com/presentation/236706280/Chapter-8-Ion-Implantation-II [Accessed 26 Jul. 2016].

[7] cfamm.ucr.edu. (2017). *Brief Introduction To Scanning Electron Microscopy*. [online] Available at: http://cfamm.ucr.edu/documents/sem-intro.pdf [Accessed 26 Apr. 2017].

[8] Krumeich, F. (n.d.). *Properties of Electrons, their Interactions with Matter and Applications in Electron Microscopy*. [online] microscopy.ethz.ch. Available at: http://www.microscopy.ethz.ch/downloads/Interactions.pdf [Accessed 24 Apr. 2017].

[9] Nanoscience.com. (2017). *Sample-Electron Interaction for SEM*. [online] Available at:http://www.nanoscience.com/technology/sem-technology/sample-electron-interaction/ [Accessed 1 May 2017].

[10] Google.co.za. (2017). *Google*. [online] Available at: https://www.google.co.za/?gws_rd=ssl#q=www.researchgate.net/Figure/257031300_fig5_Fig-5-RBS-spectrum-and-%09RUMP-simulation-of- annealed-SnO-2-film&* [Accessed 17 Feb. 2017].

[11] Dileepnanotech.com. (2011). *Micro and Nanofabrication of Gold Structures on Silicon Substrate*. [online] Available at: http://www.dileepnanotech.com/articles/Lithography.html [Accessed 17 Feb. 2017].

Chapter 5

EXPERIMENTAL PROCEDURE

In this chapter the experimental procedure is outlined. A description of how the samples were prepared before and after implantation is given. A procedure how the samples were cut into smaller pieces for experimental analysis also given.

Sample preparation

The starting materials for this project were single crystalline 6H-SiC wafers from Valley Design Corporation, with diameter 50.8 mm, thickness 368 ± 25 μm and a micro-pipe area density <30 cm^{-2} . The 6H-SiC wafers was cut into two halves using a diamond scriber. These samples were cleaned four times in an ultra-sonic bath with acetone. Each cleaning cycle took 10 minutes. This was followed by rinsing with de-ionised water and finally dry blown with nitrogen. After this cleaning procedure the samples were sent for implantation.

Implantations

The implantations of all samples were performed at the Institut für Festkörperphysik, Friedrich-Schiller-Universität, Jena, Germany. The implantations were carried out with 360 keV europium ions at 600 ºC with a fluence of 1×10^{16} cm^{-2} for the study of radiation damage and diffusion of europium. To avoid channelling, implantation was done at an angle of 7^{o} relative to normal incidence. Beam induced target heating (during implantation) was minimised by keeping the flux below 10^{-13} $cm^{-2}s^{-1}$. The vacuum pressure was kept at about 10^{-4} Pa. After implantation, the samples were further cut into 8×8 mm^2 and further cleaned with acetone prior analysis with RBS-C, SEM and heat treatment/annealing. Some of the as-implanted samples were annealed at temperatures from 1000 to 1400 °C for 5 hrs in steps of 100 °C.

The annealing

For the annealing process, a computer controlled Webb 77 graphite furnace was used. Samples were analysed after each annealing cycle. The sample was put inside a graphite crucible and then loaded into the oven. This was applied in every annealing cycle, and the

reason for that is that the contamination of the annealing sample by other elemental residues that may be stuck in the furnace walls must be avoided. This kind of contamination is very possible since the furnace is used by different researchers for various studies.

The oven was always evacuated to lower pressure of about 10^{-6} mbar after loading the sample. The oven was then degassed at 100 °C for 3 hours before starting with the annealing process. This ensures that the maximum pressure during annealing is kept at 10^{-5} mbar and the pumping time is reduced. The temperature is controlled by a Eurotherm 2704 controller that is connected to a thermocouple and a pyrometer. An average value is measured.

During the heating process the vacuum pressure increases from 10^{-6} to 10^{-5} mbar. The heating rate of this machine was kept at around 20 °C/min. The heating element heats up to a selected temperature level and then stays there for 5 hours. At the end of annealing the current is switched off and the system cools down. The vacuum is brought down by switching off the high vacuum pump and then the vacuum is finally broken completely by opening argon gas into the chamber to bring the pressure to the atmospheric pressure. A sample is removed and then analysed.

The depth profiles of implanted Eu were obtained by RBS at room temperature by production of a collimated beam of particles with energy of 1.4 and 1.6 MeV at a scattering angle of 165^{o} using the accelerator at the University of Pretoria. The analysing beam was collimated to a spot of 1mm in diameter and the current was kept below 15 nA to avoid pile-up and over-heating of the target sample. To suppress secondary electrons, an electrode was kept at a negative potential of 100 V in front of the target. An integrated charge of 8 μC was collected to ensure sufficient counting statistics.

A surface barrier detector telescope was placed at a scattering angle of 165^{o} for the detection of backscattered particles. Aligned spectra were normalised to random spectra collected during rotation of the sample about an axis tilted by approximately 5^{o} relative to the channelling direction.

The same set-up was also used to investigate radiation damage in the single crystalline samples by Rutherford backscattering spectrometry in a channelling mode spectrometry (RBS-C). The backscattered energy in channels were converted into depth (in nm) using the energy loss data and the density of pristine SiC i.e. 3.21 gcm^{-3}.

Samples surfaces before and after annealing were investigated by field emission scanning electron microscopy (FEG-SEM) at the University of Pretoria, employing a Zeiss Ultra 55 instrument fitted with the usual SEM detectors and an in-lens detector.

Chapter 6

RESULTS AND DISCUSSION

The migration behavior of europium implanted into 6H-SiC was investigated using Rutherford backscattering spectrometry (RBS), (RBS-C) and scanning electron microscopy(SEM). This chapter presents and discusses the results and is organized as follows: Section 6.1 and 6.2 present and discuss radiation damage and diffusion results respectively.

6.1. **Radiation Damage Results**

Typical RBS spectra (both Random and aligned) of Eu ions implanted into 6H-SiC at 600 °C are shown in Figure.6.1. The un-implanted 6H-SiC (virgin) spectrum is included for comparison. Arrows in Figure 6.1 indicate the surface energy positions in channels of the elements. Implantation at 600 °C resulted in the appearance of the broad peak around channel 230. This peak indicates the amount of radiation damage retained after implantation. The aligned spectrum in Figure 6.1 does not overlap with the random spectrum, indicting the absence of amorphous material. The lack of amorphization is due to the availability of thermal energy to the displaced atoms that increase the probability of recombination during implantation at this temperature. Similar results have been reported for other implanted FPs surrogates at the same implantation temperature [1-7].

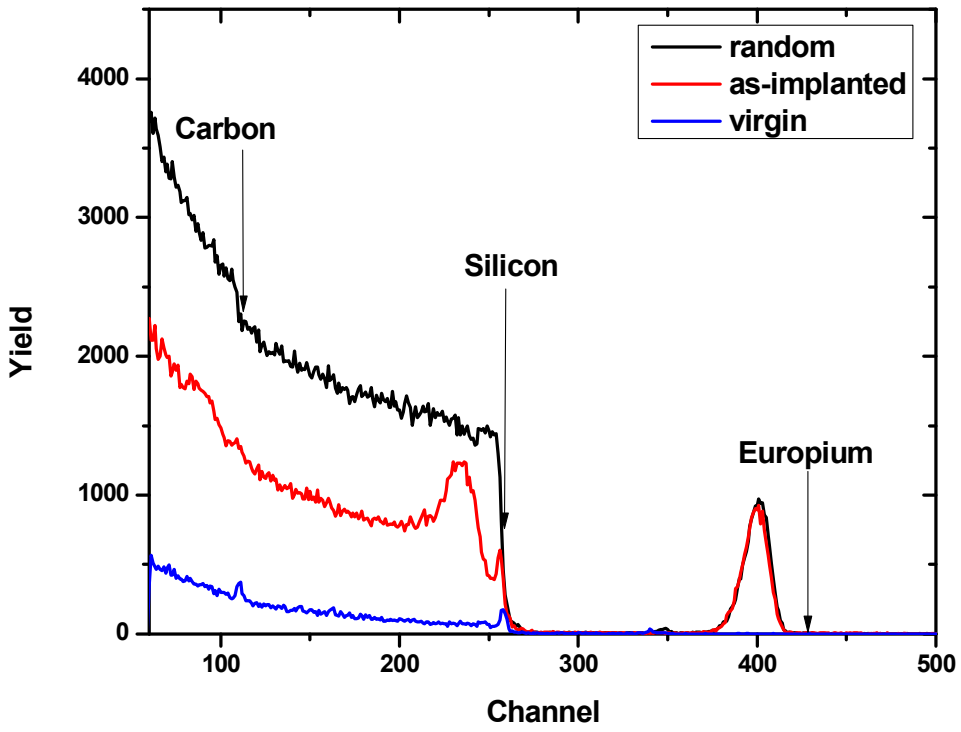

Figure 6.1: *Rutheford backscattering spectrometry (RBS) spectra of 6H-SiC implanted with 360 keV Eu ions (both random and aligned) at 600 ºC and the virgin SiC.*

The measured Eu depth profile (from RBS), the TRIM simulated Eu depth profile using SRIM 2012 [8] and displacement per atom (*dpa*) are shown in Figure 6.2. The ion fluence was converted into displacement per atom (*dpa*) by:

$$dpa = \frac{\frac{V_{ac}}{ion(cm)} \times 10^{8} \times \varphi(ions.cm^{-2})}{\rho_c(ions.cm^{-3})} \qquad (6.1)$$

where φ is the ion fluence, ρ_c is the theoretical density of silicon carbide (9.641 atm/cm^3) and v_{ac}/ion(cm) is the vacancy per ion ratio obtained from SRIM 2012 [8].

The projected range of measured Eu depth profile is in reasonable agreement with the SRIM simulation, while the as-implanted profile is broader than the simulated due to SRIM approximations. The TRIM approximations includes a binary collision between ion and target, neglecting the recombination of atoms with vacancies, the interatomic potential as a universal form. The defects are closer to the surface as compared to the implanted Eu profile. This is because (as literature has proven on silicon self-diffusion), silicon interstitials (Si_I) vacancies proceed preferentially toward the surface [9].

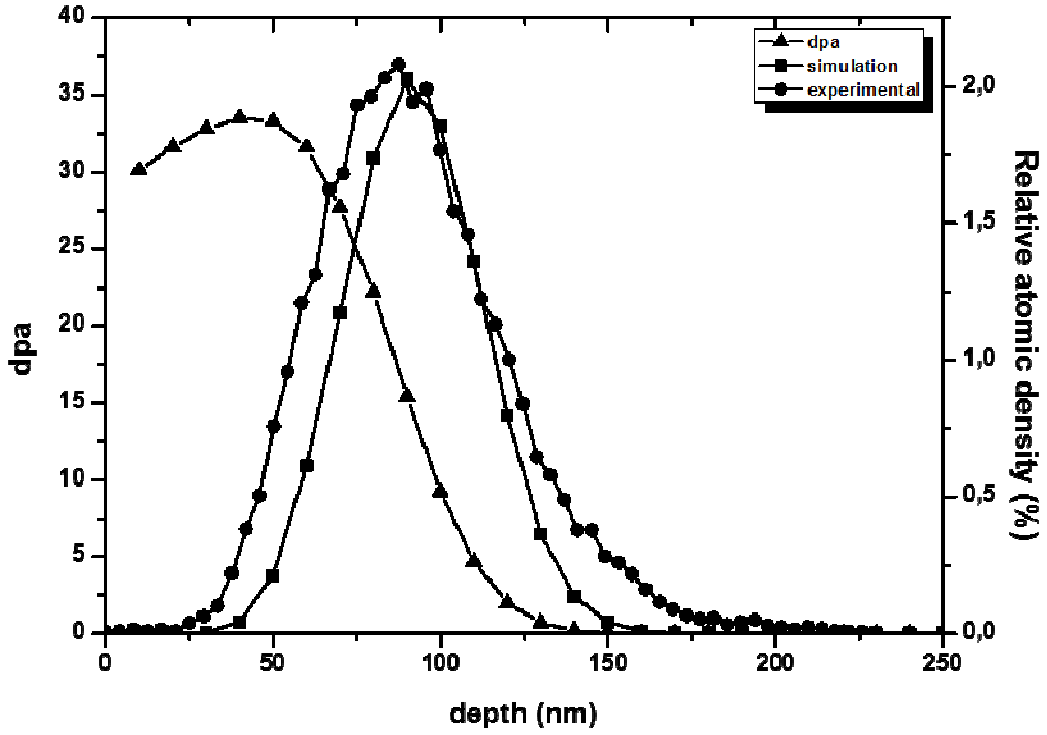

Figure 6.2: *The as-implanted Eu (360 keV) depth profile (from RBS), TRIM simulated Eu depth profile and displacement per atom (dpa).*

The aligned silicon depth profiles of the implanted 6H-SiC after isochronal annealing at 1000, 1100, 1200, 1300 and 1400 °C for 5 hours are shown in Figure 6.3 (the random, virgin and as implanted spectra are included for comparison). The projected range (R_p) of the radiation damage peak is about 98 nm. Annealing at 1000 ºC caused some reduction in the radiation damage peak, indicating some annealing of radiation damage at this temperature. This reduction of radiation damage was more pronounced at 1100 ºC, indicating further annealing. The radiation damage peak was further reduced after annealing at 1200 ºC indicating a continued annealing of radiation damage. The peak completely disappeared after annealing at 1300 and 1400 ºC. Even though the reduction of radiation damage within the lattice is significant after annealing at 1400 ºC, the aligned spectrum of the annealed sample is still higher than the un-implanted (virgin) aligned spectrum. This indicates that the total annealing of radiation damage was not achieved after annealing at 1400 ºC. From these results, it is evident that in order to anneal all the radiation damage retained after implantation at 600 ºC during isochronal annealing experiments (similar to this study), a temperature greater than 1400 ºC is required.

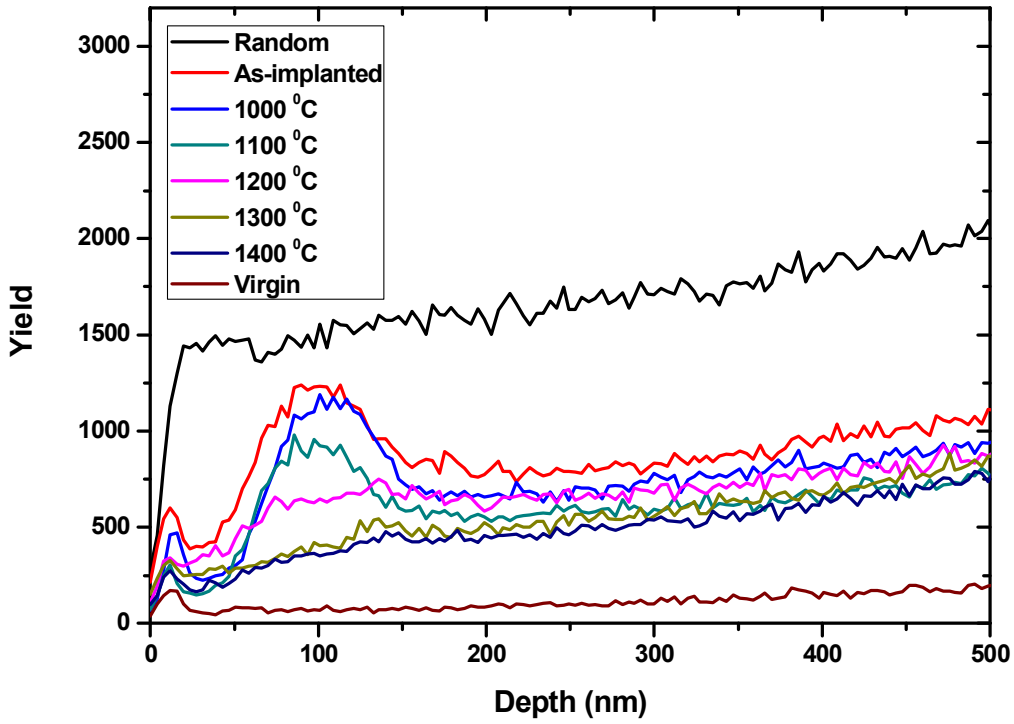

Figure 6.3: *Si depth profile of Eu implanted into SiC by 360 keV Eu ions and annealed at various temperatures.*

6.2. Diffusion Results

Figure 6.4 shows the aligned silicon depth profile in SiC implanted with Eu ions, random and Eu depth profiles are included. These results clearly indicate that, the as-implanted Eu is initially embedded in the highly defective radiation damage region. The migration behaviour of Eu implanted into 6H-SiC was investigated simultaneously with the annealing of radiation damage. The Eu depth profiles obtained from RBS after isochronal annealing are shown in Figure 6.5 (the as-implanted profile is included for comparison).

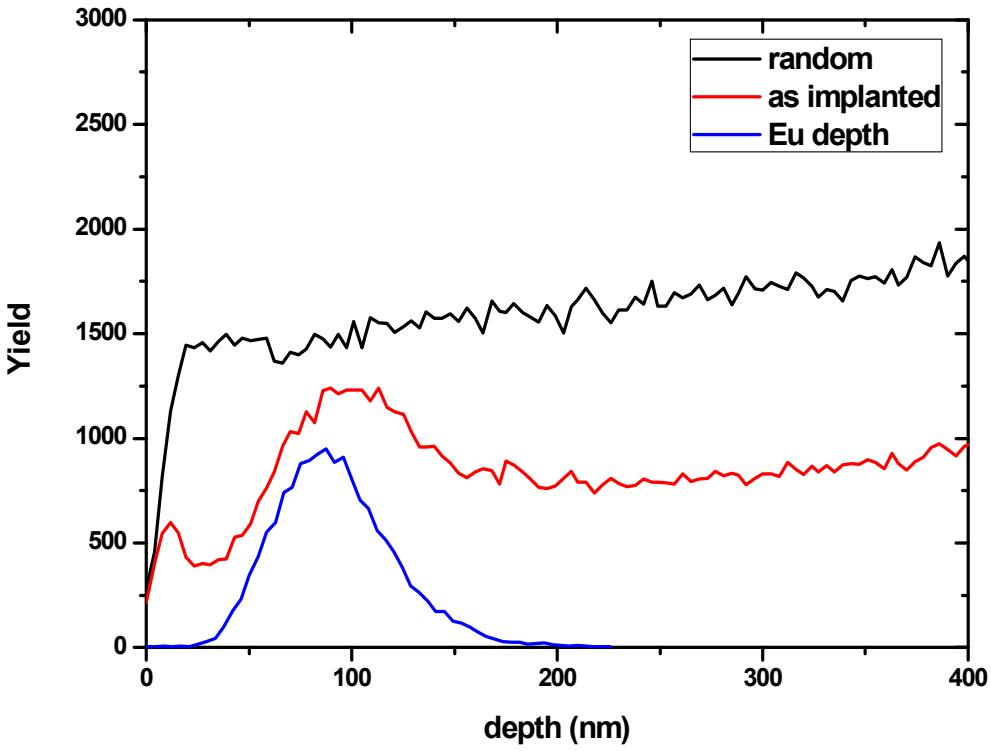

Figure 6.4: *Si depth profile of Eu ions implanted into 6H-SiC indicating Eu profile peak within the damaged area of Si.*

Annealing at 1000 ºC resulted into a shift of Eu peak towards the surface, indicating the migration of Eu towards the surface was already taking place (see Figure 6.6(c)). At 1100 ºC, the peak shift towards the surface became more significant. At 1200 and 1300 ºC, there was no peak shift until at 1400 ºC where a further peak shift was observed.

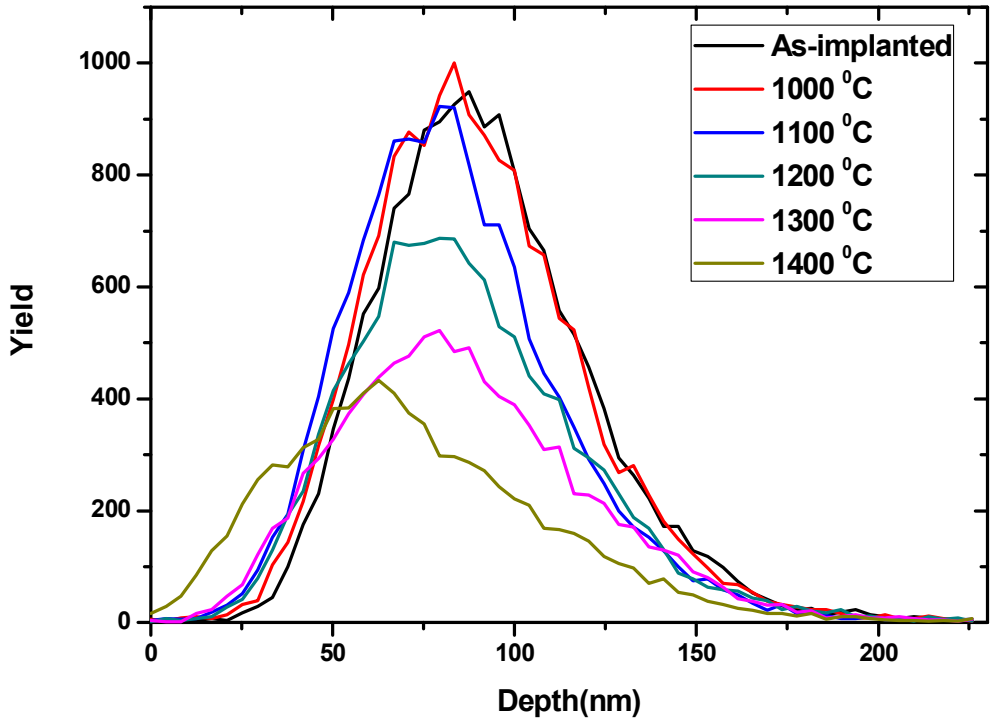

Figure 6.5: Eu *depth profiles of Eu implanted into 6H-SiC at 600 °C after isochronal annealing at various temperatures for 5hours.*

The retained ratios were calculated as the ratio of the area of Eu counts after annealing to that of as-implanted and the results are illustrated in Figure 6.6(a). The retained ratio reveals that the migration of Eu towards the surface was accompanied by a subsequent loss of implanted Eu from the surface at annealing temperatures above 1000°C. About 10% of Eu was lost after annealing at 1100 °C and about 50% was lost after annealing at 1300 and 1400 °C.

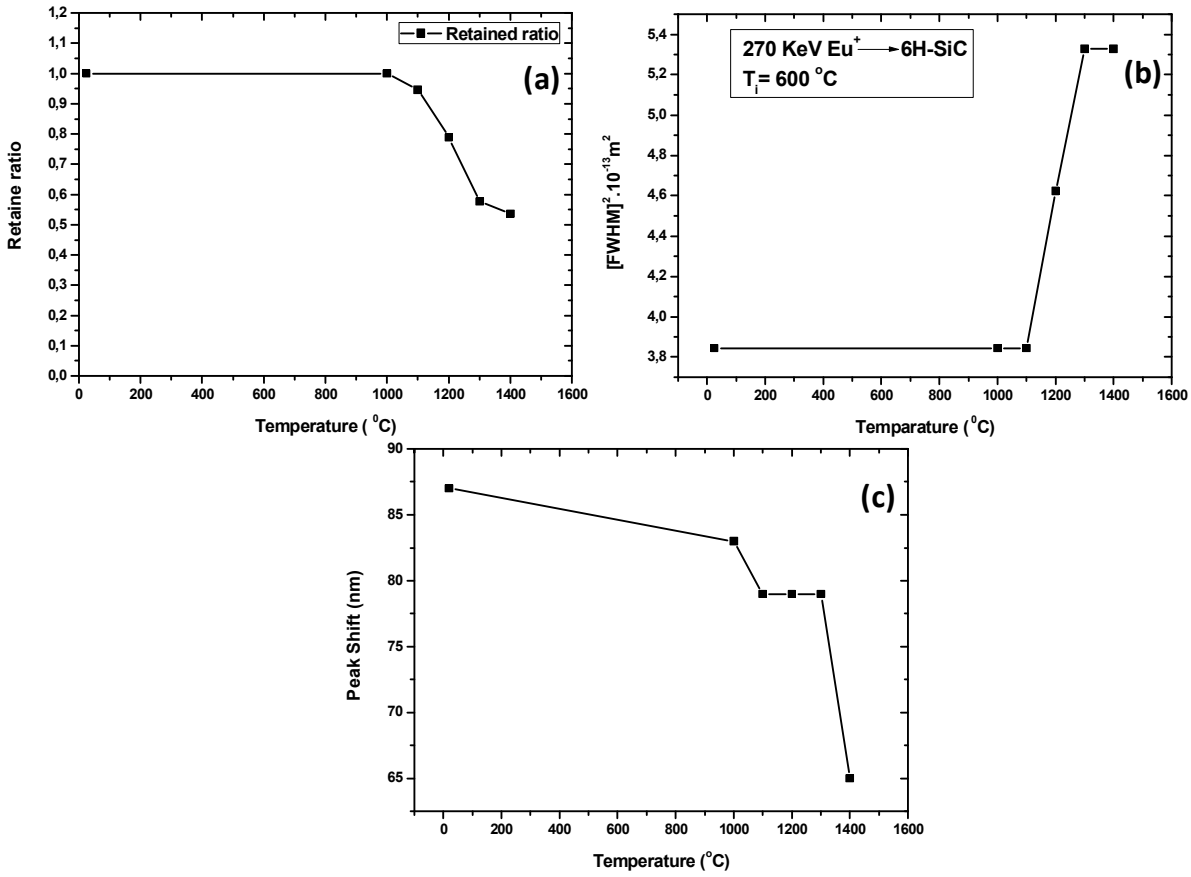

Figure 6.6: (a) *Retained ratio of Eu implanted into 6H-SiC at 600 °C after isochronal annealing at different temperatures for 5 hours. (b) Full width at half maximum plotted as a function of temperature for 360 keV of Eu ions in 6H-SiC implanted at 600 °C after isochronal annealing at different temperatures for 5 hours. (c) Peak shift of the Eu profile of the as-implanted and annealed samples at 1000 to 1400 °C in steps of 100 °C.*

The diffusion of implanted Eu was investigated by comparing the full width at half maximum (FWHM) of the Eu depth profiles of the as-implanted and the annealed samples. The FWHMs square is plotted as a function of temperature in Figure 6.6(b). The FWHM obtained after annealing at 1000 to 1100 ºC, showed no broadening indicating no detectable Fickian diffusion after annealing at these temperatures. However, the Eu peak shifted towards the surface as observed in Figure 6.6(c). The broadening of the FWHM was observed after annealing at 1200 and 1300 °C indicating the beginning of Fickian diffusion at these temperatures. Annealing at 1400 °C showed no broadening of the FWHM. No further Eu peak shifts (as compare to 1100 °C) was observed at 1200 and 1300 °C, indicating that the Eu loss was purely due to Fickian diffusion, while a further shift was observed at 1400 °C

The shift of Eu peak towards the surface combined with annealing of radiation damage, may be due to trapping and de-trapping of Eu implants by radiation damage. On the as-implanted samples Eu is trapped by radiation damage retained after implantation. As these radiation damage are annealed, de-trapping of Eu occurs which allows the Eu to shift towards the surface. This process progresses with increasing temperature until the temperature where diffusion take place.

The surface topography of the as-implanted compared with annealed samples are shown in Figure 6.7. The as-implanted samples were fairly smooth. No major changes were observed after annealing up to 1200 °C. These results indicate that the shift towards the surface after annealing up until 1100 °C was not due to the changes in the samples' surface. This confirms the trapping and de-trapping of implants theory suggested earlier. The SEM images also show the appearance of step bunches on the surface after annealing at 1300 and 1400 ºC. This is due to thermal etching of the material during annealing [10]. However, this thermal etching took place at lower temperatures than the one at which it occurred (1500ºC) in Ref. [10]. This is due to the damage introduced into the surface region of the 6H-SiC after ion bombardment. Such damage lowers the surface binding energy resulting in increased thermal etching. The peak broadening was not observed after annealing at 1400 ºC but the shift and loss of Eu was considerably higher than at the other higher annealing temperatures. This can be due to the severe surface changes of the sample after annealing at this temperature (see fig 6.7).

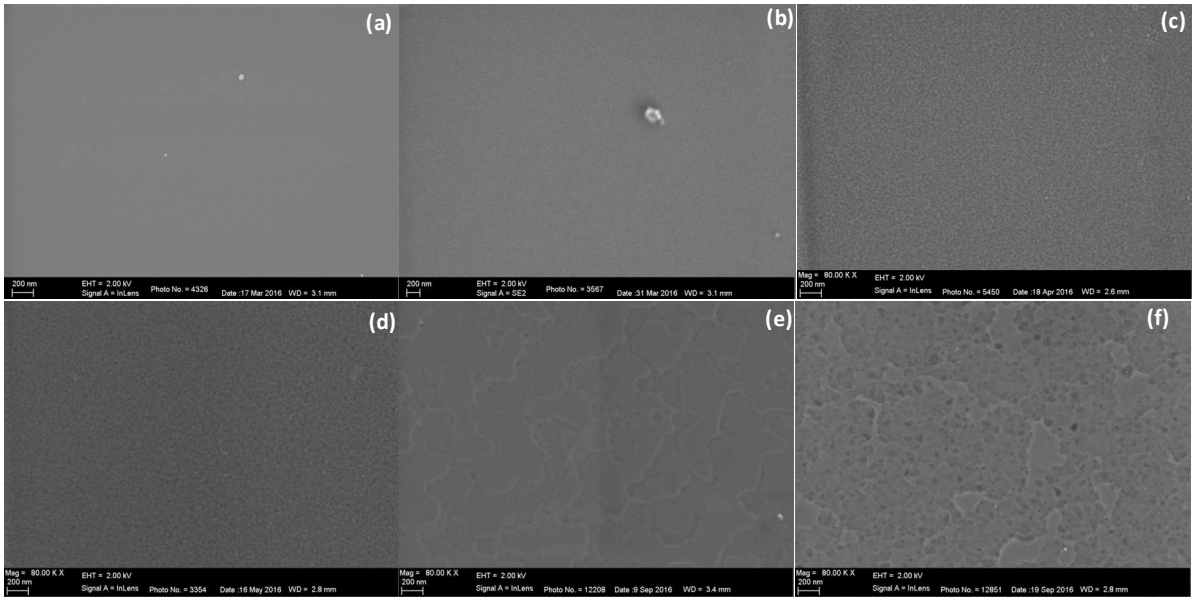

Figure 6.7: *SEM images of Eu ions implanted into 6H–SiC at 600 °C: (a) as-implanted, subsequently annealed at (b) 1000, (c) 1100, (d) 1200, (e)1300 and (f) 1400 °C.*

The diffusion coefficients were estimated from the broadening of FWHM of Eu depth profile after annealing at 1200 and 1300 °C as explained in chapter 2 (using equation 2.5). The diffusion coefficients at 1200 and 1300 °C were found to be $1.56 \times 10^{-18}\ m^2/s$ and $2.98 \times 10^{-18}\ m^2/s$ respectively. On the other hand, Dwaraknath et al.[11], found that the diffusion coefficients of Eu in SiC at 1200 and 1300 °C were $1.4 \times 10^{-20}\ m^2/s$ and $2.6 \times 10^{-19}\ m^2/s$ respectively. The differences between the diffusion coefficients may be due to the different conditions used in the two studies. In this study, Eu introduced radiation damage directly to SiC due to the direct implantation while Dwaraknath implanted the fission products (FPs) into a pyrolitic carbon layer (PyC) which was placed between the high purity CVD β-SiC and a coating of plasma-enhanced CVD SiC. This ensured that the fission products resided in the interface and not directly in the SiC substrate. Because of these different conditions, a different amount of FP will diffuse in a given period of time even at the same temperatures.

The plot of lnD as a function of 1000/T(K) is shown in Figure 6.8. Using P_1 and P_2 of the graph the slope was calculated from which the activation energy E_a was deduced and consequently D_0 was estimated from the y-intercept. The values for E_a and D_0 were found to be $1.20 \times 10^{-3}\ eV$ and $3.08 \times 10^{-18}\ m^2/s$ respectively. This fitting of a straight line to only two points, is highly controversial and can, at best, only give order of magnitude values to the fitting parameters. In comparison, the values for Dwaraknath et al [11], are 5.5 eV and $1.2 \pm 0.25\ m^2/s$. The difference with our values might be due to our inaccurate fitting to two points and/or the difference in conditions. One can expect that in-diffusion through a surface resulting in the diffusion species to overcome the surface energy might result in lower diffusion coefficients as found by Dwaraknath et al.[11] and consequently different values for E_a and D_0.

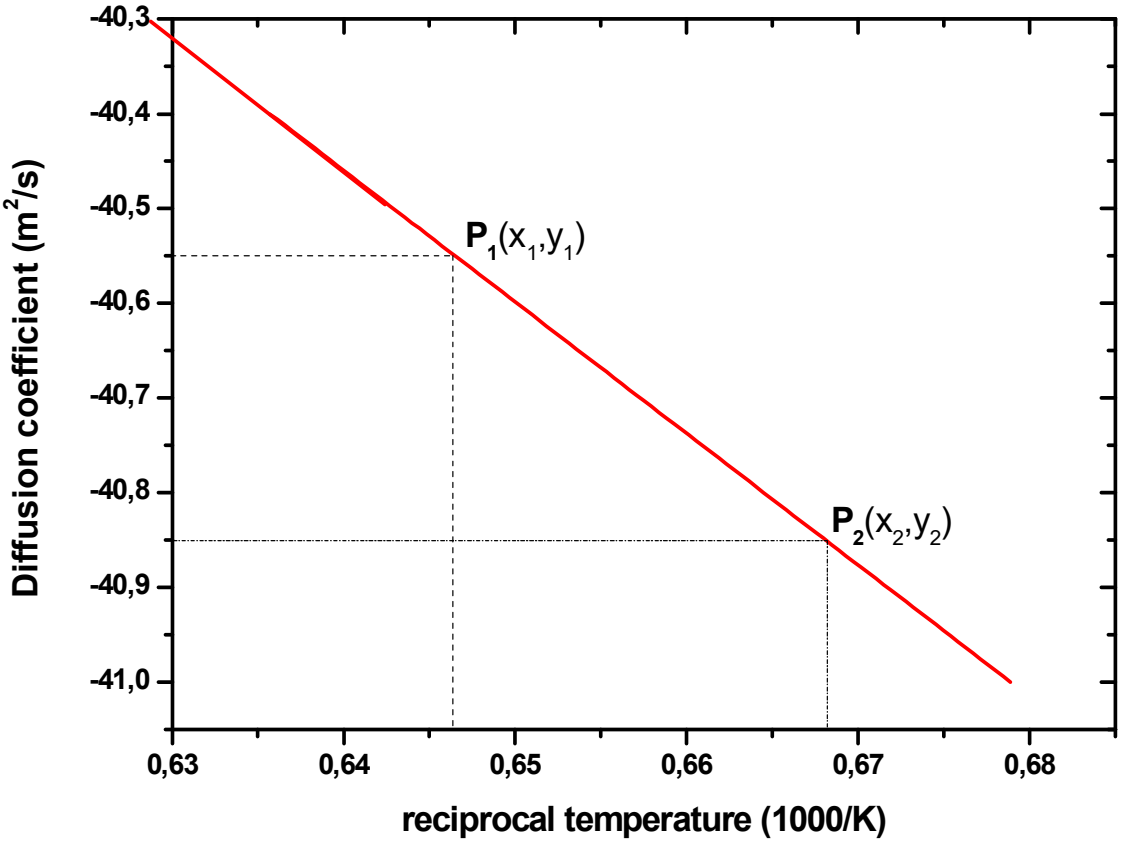

Figure 6.8: *A graph of lnD vs 1/T for 1200 and 1300 °C annealing temperatures of a Eu implanted at 600 °C in 6H-SiC.*

Normally the nuclear fuel particles/rods are replaced after every 18 to 24 months [12]. The time taken by Eu to migrate through the thickness of SiC was calculated using equation 6.2:

$$t = \frac{x^2}{D} \qquad (6.2)$$

where x is the thickness of SiC layer in the TRISO particle, viz. $x = 35\mu m$, D is the diffusion coefficient.

At 1200 °C, the diffusion coefficient suggests that it would take approximately 25 years for Eu to migrate through this thickness while it suggests that it would take 13 years at 1300 °C. Therefore, our results suggest that in TRISO particle, Eu does not only migrate via diffusion mechanism investigated in this study. This discrepancy might be true if one considers the following facts about the TRISO particle in a nuclear reactor:

- Chemical vapour deposition (CVD) is used to manufacture the layers in the TRISO particle. This will result in polycrystalline SiC which will have different diffusion coefficients at the different temperature than the single crystal SiC used in this study.
- TRISO particles are continuously exposed to different irradiation during reactor operation. Thus radiation-enhanced diffusion of the Eu may occur.
- Different fission products exist in the TRISO particle. This may result in synergistic effects [13]

References

[1] Friedland, E., Malherbe, J.B., van der Berg, N.G., Hlatshwayo, T.T., Botha, A.J., Wendler, E. and Wesch, W. (2009). Study of silver diffusion in silicon carbide.*Journal of Nuclear Materials*, 389(2), pp.326-331.

[2] Friedland, E., van der Berg, N.G., Malherbe, J.B., Kuhudzai, R.J., Botha, A.J., Wendler, E. and Wesch, W. (2010). Study of iodine diffusion in silicon carbide.*Nuclear Instruments and Methods in Physics Research Section B: Beam Interactions with Materials and Atoms*, 268(19), pp.2892-2896.

[3] Friedland, E., van der Berg, N.G., Hlatshwayo, T.T., Kuhudzai, R.J., Malherbe, J.B., Wendler, E. and Wesch, W. (2012). Diffusion behavior of cesium in silicon carbide at T>1000°C.*Nuclear Instruments and Methods in Physics Research Section B:Beam Interactions with Materials and Atoms*, 286, pp.102-107.

[4] Malherbe, J.B., van der Berg, N.G., Botha, A.J., Friedland, E., Hlatshwayo, T.T., Kuhudzai, R.J., Wendler, E., Wesch, W., Chakraborty, P. and da Silveira, E.F. (2013). SEM analysis of ion implanted SiC. *Nuclear Instruments and Methods in Physics Research Section B: Beam Interactions with Materials and Atoms*, 315, pp.136-141.

[5] Friedland, E., Hlatshwayo, T.T., van der Berg, N.G. and Mabena, M.C. (2015). Influence of radiation damage on krypton diffusion in silicon carbide. *Nuclear Instruments and Methods in Physics Research Section B: Beam Interactions with Materials and Atoms*, 354, pp.42-46.

[6] Friedland, E., van der Berg, N.G., Hlatshwayo, T.T., Kuhudzai, R.J., Malherbe, J.B.,Wendler, E. and Wesch, W. (2012). Diffusion behavior of cesium in siliconcarbide at T>1000°C.*Nuclear Instruments and Methods in Physics Research Section B: Beam Interactions with Materials and Atoms*, 286, pp.102-107.

[7] Friedland, E., Hlatshwayo, T.T. and van der Berg, N.G. (2013). Influence of radiation damage on diffusion of fission products in silicon carbide. *physica status solidi(c)*, 10(2), pp.208-215.

[8] Software Informer. (2017). *SRIM 2012.0 Download (Free) - SRIM 2008.exe*.[online] Available at: http://srim.software.informer.com/2012.0/ [Accessed 19 Mar. 2017].

[9] Ghibaudo, G. and Christofides, C. (1997). *Effect of disorder and defects in ion-implanted semiconductors*. San Diego: Academic Press.

[10] Hlatshwayo, T.T., Malherbe, J.B., van der Berg, N.G., Botha, A.J. and Chakraborty, P.(2012). Effect of thermal annealing and neutron irradiation in 6H-SiC implanted with silver at 350°C and 600°C. *Nuclear Instruments and Methods in Physics Research Section B: Beam Interactions with Materials and Atoms*, 273, pp.61-64.

[11] Dwaraknath, S.S. and Was, G.S. (2016). The diffusion of cesium, strontium, and europium in silicon carbide.*Journal of Nuclear Materials*, 476,pp.155-167.

[12] World-nuclear.org. (2017). *Nuclear Fuel Cycle Overview - World Nuclear Association*. [online] Available at:http://www.world-nuclear.org/information-library/nuclear-fuel-cycle/introduction/nuclear-fuel-cycle-overview.aspx[Accessed 30 May 2017].

[13] R.J. Kuhudzai, J.B. Malherbe, T.T. Hlatshwayo, N.G. van der Berg, A. Devaraj, Z. Zhu and M. Nandasiri, Synergistic effects of iodine and silver ions co-implanted in 6H-SiC, J. Nucl. Mater. 467 (2015) 582-587.

[14] Kachurin, G.A., Tyschenko, I.E. and Fedina, L.I. (1992). High-temperature ion implantation in silicon.*Nuclear Instruments and Methods in Physics Research Section B: Beam Interactions with Materials and Atoms*, 68(1-4), pp.323-330.

Chapter 7

Summary and Future studies

This study focused on the migration behaviour of Eu implanted into 6H-SiC at 600 ºC. Implantation temperature retained crystallinity of 6H-SiC with some defects. This was expected as the implantation temperature was above the critical temperature of SiC amorphization. Reduction of radiation damage retained after implantation, already took place after annealing at 1000 °C. This annealing of radiation damage progressed with increasing annealing temperature up to 1400 °C. The shift of Eu towards the surface was already taking place after annealing at 1000 °C and became more pronounced with increasing temperature (where it was accompanied by Eu loss from the surface). Fickian's diffusion of Eu was only observed after annealing at 1200 °C and continued up until 1300 °C. No Fick's diffusion was observed after annealing at 1400 °C. The shift of Eu profiles after annealing from 1000 to 1200 °C was explained using trapping and de-trapping of the implanted ions by defects. A further shift of Eu at 1400 °C was due to thermal etching of the surface.

These results imply that Eu diffusion is controlled by radiation retained after implantation. In a nuclear environment where continuous irradiation of SiC is taking place, these result are of crucial important. To get holistic image of the migration behaviour of Eu in SiC, the following study must be conducted:

- The migration behaviour of Eu in Polycrystalline chemical vapour deposited (CVD) need to be investigated.
- The effect of different irradiation in the migration behaviour of Eu in both single crystalline and polycrystalline SiC need to be investigated.
- The synergetic effect of other fission products in the migration behaviour of Eu in SiC need to be investigated.